A generalized class of strongly stable and dimension-free T-RPMD integrators

Cite as: J. Chem. Phys. **154**, 024106 (2021); https://doi.org/10.1063/5.0036954 Submitted: 10 November 2020 . Accepted: 07 December 2020 . Published Online: 08 January 2021

Jorge L. Rosa-Raíces, Jiace Sun, D Nawaf Bou-Rabee, and D Thomas F. Miller







View Online

ARTICLES YOU MAY BE INTERESTED IN

Dimension-free path-integral molecular dynamics without preconditioning
The Journal of Chemical Physics 152, 104102 (2020); https://doi.org/10.1063/1.5134810

Cayley modification for strongly stable path-integral and ring-polymer molecular dynamics The Journal of Chemical Physics 151, 124103 (2019); https://doi.org/10.1063/1.5120282

OrbNet: Deep learning for quantum chemistry using symmetry-adapted atomic-orbital features

The Journal of Chemical Physics 153, 124111 (2020); https://doi.org/10.1063/5.0021955





A generalized class of strongly stable and dimension-free T-RPMD integrators

Cite as: J. Chem. Phys. 154, 024106 (2021); doi: 10.1063/5.0036954 Submitted: 10 November 2020 • Accepted: 7 December 2020 • Published Online: 8 January 2021







Jorge L. Rosa-Raíces, Jiace Sun, Nawaf Bou-Rabee, and Thomas F. Miller III (1)

AFFILIATIONS

- Division of Chemistry and Chemical Engineering, California Institute of Technology, Pasadena, California 91125, USA
- ²Department of Mathematical Sciences, Rutgers University Camden, Camden, New Jersey 08102, USA
- a) Electronic mail: nawaf.bourabee@rutgers.edu
- b) Author to whom correspondence should be addressed: tfm@caltech.edu

ABSTRACT

Recent work shows that strong stability and dimensionality freedom are essential for robust numerical integration of thermostatted ring-polymer molecular dynamics (T-RPMD) and path-integral molecular dynamics, without which standard integrators exhibit non-ergodicity and other pathologies [R. Korol et al., J. Chem. Phys. 151, 124103 (2019) and R. Korol et al., J. Chem. Phys. 152, 104102 (2020)]. In particular, the BCOCB scheme, obtained via Cayley modification of the standard BAOAB scheme, features a simple reparametrization of the free ring-polymer sub-step that confers strong stability and dimensionality freedom and has been shown to yield excellent numerical accuracy in condensed-phase systems with large time steps. Here, we introduce a broader class of T-RPMD numerical integrators that exhibit strong stability and dimensionality freedom, irrespective of the Ornstein–Uhlenbeck friction schedule. In addition to considering equilibrium accuracy and time step stability as in previous work, we evaluate the integrators on the basis of their rates of convergence to equilibrium and their efficiency at evaluating equilibrium expectation values. Within the generalized class, we find BCOCB to be superior with respect to accuracy and efficiency for various configuration-dependent observables, although other integrators within the generalized class perform better for velocity-dependent quantities. Extensive numerical evidence indicates that the stated performance guarantees hold for the strongly anharmonic case of liquid water. Both analytical and numerical results indicate that BCOCB excels over other known integrators in terms of accuracy, efficiency, and stability with respect to time step for practical applications.

Published under license by AIP Publishing. https://doi.org/10.1063/5.0036954

I. INTRODUCTION

Path-Integral Molecular Dynamics (PIMD) provides a practical and popular tool to simulate condensed-phase systems subject to strong nuclear quantum effects. ^{1–3} Based on the ring-polymer correspondence between quantum and classical Boltzmann statistics, ^{4,5} PIMD exploits the computational methods of molecular dynamics ^{6–9} to approximate quantum thermodynamics and kinetics through various classical models. ^{10–15} Applications of PIMD include calculations of chemical reaction rates, ^{16,17} diffusion coefficients, ^{18,19} absorption spectra, ^{20,21} solid and liquid structure, ^{22,23} and equilibrium isotope effects. ^{24,25}

Many numerical integration schemes for PIMD are based on a symmetric Trotter (i.e., Strang) splitting 26,27 of the exact

time-evolution operator and feature a sub-step for free ring-polymer propagation. ^{28–30} Due to fast harmonic motions present in the free ring polymer, a *strongly stable* implementation of this substep is essential. ^{31,32} Strong stability can be achieved by one of two approaches. The first approach introduces a preconditioned form of the equations of motion by modifying the ring-polymer mass matrix. Preconditioning improves the stability of the exact free ring-polymer update at the expense of consistent dynamics. ^{28,30,33–36} The second approach does not modify the ring-polymer mass matrix, leaving the dynamics non-preconditioned, ^{29,37–40} and instead replaces the exact free ring-polymer update with a strongly stable approximation. ⁴¹ We apply the latter approach in the current work to Thermostatted Ring-Polymer Molecular Dynamics (T-RPMD), ³⁸ a non-preconditioned variant of PIMD featuring an Ornstein-Uhlenbeck

thermostat that approximately preserves the real-time dynamical accuracy of RPMD for quantum correlation functions of a wide range of observables.4

In addition to strong stability of the free ring-polymer update, another basic requirement of a numerical integrator for T-RPMD is the non-zero overlap between the numerically sampled and exact ring-polymer configurational distributions in the limit of an infinite number of ring-polymer beads. Standard integrators fail to satisfy this requirement at any finite integration time step, 43 which motivates the introduction of dimension-free T-RPMD schemes that allow for accurate configurational sampling with large time-stepping and arbitrarily many ring-polymer beads. We recently found that standard integrators could be made dimension-free through the introduction of a suitable strongly stable ring-polymer update,⁴³ and the current paper investigates this finding in much greater

To this end, we introduce a function θ that defines the free ring-polymer update and deduce how the choice of θ impacts the properties and performance of the corresponding T-RPMD integrator. The case $\theta(x) = x$, i.e., θ is the identity, corresponds to the exact free ring-polymer update. Therefore, to ensure secondorder accuracy, θ must approximate the identity near the origin, i.e., $\theta(0) = 0$, $\theta'(0) = 1$, and $\theta''(0) = 0$. Moreover, strong stability requires that the range of the function θ is within $(0, \pi)$ for x > 0, and ergodicity and dimensionality freedom of the corresponding T-RPMD integrator impose additional requirements on θ . There are many choices of θ that fulfill the identified requirements including $\theta(x) = 2 \arctan(x/2)$, which leads to the BCOCB scheme introduced in Ref. 43. In fact, we find that this choice of θ is superior for the estimation of configurational averages via T-RPMD from the perspectives of accuracy and efficiency, despite its poor performance with respect to the ring-polymer velocities.

This paper is organized as follows. In Sec. II, we recall exact T-RPMD and its time discretization, present the new function θ that determines the free ring-polymer update, and obtain sufficient conditions on θ to guarantee strong stability and dimensionality freedom of the corresponding T-RPMD integrator. In Sec. III, we compare the performance of various θ in applications to the one-dimensional quantum harmonic oscillator and to a quantummechanical model of room-temperature liquid water. Section IV summarizes the work, and appendixes provide supporting mathematical proofs and computational protocols.

II. THEORY

A. T-RPMD

Consider a one-dimensional quantum particle with the Hamiltonian operator

$$\hat{H} = \frac{1}{2m}\hat{p}^2 + V(\hat{q}),\tag{1}$$

where m is the particle mass, \hat{q} and \hat{p} are the position and momentum operators, and $V(\hat{q})$ is the potential energy surface. Ignoring exchange statistics, the properties of this system at thermal equilibrium are encoded in the quantum partition function,

$$Q = \operatorname{tr}[e^{-\beta \hat{H}}], \tag{2}$$

where $\beta = (k_B T)^{-1}$, k_B is the Boltzmann constant, and T is the physical temperature. Using a path-integral discretization (i.e., a Trotter factorization of the Boltzmann operator²⁶), $Q = \lim_{n \to \infty} Q_n$ can be approximated by the classical partition function Q_n of a ring polymer with *n* beads,⁴

$$Q_n = \frac{m^n}{(2\pi\hbar)^n} \int d^n \mathbf{q} \int d^n \mathbf{v} e^{-\beta H_n(\mathbf{q}, \mathbf{v})}, \qquad (3)$$

where $q = [q_0 \cdots q_{n-1}]^T$ is the vector of bead positions and v is the corresponding vector of velocities. The ring-polymer Hamiltonian is given by

$$H_n(\boldsymbol{q}, \boldsymbol{v}) = H_n^0(\boldsymbol{q}, \boldsymbol{v}) + V_n^{\text{ext}}(\boldsymbol{q}), \tag{4}$$

which includes contributions from the physical potential

$$V_n^{\text{ext}}(\mathbf{q}) = \frac{1}{n} \sum_{j=0}^{n-1} V(q_j)$$
 (5)

and the free ring-polymer Hamiltonian

$$H_n^0(\boldsymbol{q}, \boldsymbol{v}) = \frac{m_n}{2} \sum_{i=0}^{n-1} \left[v_j^2 + \omega_n^2 (q_{j+1} - q_j)^2 \right], \tag{6}$$

where $m_n = m/n$, $\omega_n = n/(\hbar \beta)$, and $q_n = q_0$.

T-RPMD evolves the phase $[q^T v^T]^T$ of the ring polymer as per

$$\dot{\boldsymbol{q}}(t) = \boldsymbol{v}(t); \ \dot{\boldsymbol{v}}(t) = -\Omega^2 \boldsymbol{q}(t) + m_n^{-1} \boldsymbol{F}(\boldsymbol{q}(t))$$
$$-\Gamma \boldsymbol{v}(t) + \sqrt{2\beta^{-1} m_n^{-1}} \Gamma^{1/2} \dot{\boldsymbol{W}}(t), \tag{7}$$

which is a coupling of the Hamiltonian dynamics of $H_n(\mathbf{q}, \mathbf{v})$ with an Ornstein-Uhlenbeck thermostat. In Eq. (7), we introduced F(q)= $-\nabla V_n^{\text{ext}}(q)$, an *n*-dimensional standard Brownian motion W(t), and the $n \times n$ matrices

$$\Omega = U \operatorname{diag}(0, \omega_{1,n}, \ldots, \omega_{n-1,n}) U^{\mathrm{T}}$$

and

$$\Gamma = U \operatorname{diag}(0, \gamma_{1,n}, \dots, \gamma_{n-1,n}) U^{\mathrm{T}}, \tag{8}$$

where $y_{i,n} \ge 0$ is the *j*th friction coefficient, **U** is the $n \times n$ real discrete Fourier transform matrix, and the ring-polymer frequencies are given by

$$\omega_{j,n} = \begin{cases} 2\omega_n \sin\left(\frac{\pi j}{2n}\right) & \text{if } j \text{ is even} \\ 2\omega_n \sin\left(\frac{\pi (j+1)}{2n}\right) & \text{else.} \end{cases}$$
 (9)

Observe that the zero-frequency (i.e., centroid) ring-polymer mode is uncoupled from the thermostat, and the coefficients $\{y_{i,n}\}_{i=1}^{n-1}$ in Eq. (8) constitute the friction schedule applied to the non-centroid

Numerical integrators for Eq. (7) typically employ symmetric propagator splittings of the form⁴

$$e^{\Delta t \mathcal{L}_n} \approx e^{\frac{\Delta t}{2} \mathcal{O}_n} e^{\frac{\Delta t}{2} \mathcal{B}_n} e^{\frac{\Delta t}{2} \mathcal{A}_n} e^{(1-a)\Delta t \mathcal{O}_n}$$

$$\times e^{\frac{\Delta t}{2} \mathcal{A}_n} e^{\frac{\Delta t}{2} \mathcal{B}_n} e^{a\frac{\Delta t}{2} \mathcal{O}_n} \quad \text{with } a \in \{0, 1\},$$

$$(10)$$

where the operator $\mathcal{L}_n = \mathcal{A}_n + \mathcal{B}_n + \mathcal{O}_n$ includes contributions from the *n*-bead free ring-polymer motion (A_n) , the external potential (\mathcal{B}_n) , and the thermostat (\mathcal{O}_n) , and Δt is a sufficiently small time step. Note that the standard microcanonical RPMD integrator is recovered in the limit of zero coupling to the thermostat²⁹ and that Eq. (10) yields the OBABO scheme of Bussi et al. 44 if a = 1 and the BAOAB scheme of Leimkuhler⁴⁵ if a = 0.

Standard implementations of the T-RPMD splittings in Eq. (10) use the exact free ring-polymer propagator $e^{\frac{\Delta t}{2}A_n}$ to evolve the uncoupled ring-polymer modes; however, recent work by us⁴¹ showed that such implementations exhibit poor ergodicity if large numbers *n* of ring-polymer beads are employed in conjunction with large time steps Δt and suggested replacing the exact ring-polymer propagator with its Cayley approximation⁴⁷ for improved performance. Follow-up work⁴³ introduced a Cayley-modified BAOAB scheme, denoted by BCOCB, and presented numerical evidence that cemented the scheme as an improvement over standard BAOAB due to its superior equilibrium accuracy and time step stability.

Generalizing beyond the Cayley modification, the current work studies a family of modified BAOAB schemes that contains BCOCB and introduces others with similar theoretical guarantees. Specifically, the BAOAB modifications are obtained by replacing the exact free ring-polymer update in Eq. (10) with approximations that endow the properties listed below.

- (P1) Strong stability. For a free ring polymer [i.e., for V(q)= const.], the integrator with $\gamma_{j,n} = 0$ is both strongly stable and second-order accurate in Δt .
- Free ring-polymer ergodicity. For a free ring polymer, the integrator with $y_{i,n} > 0$ is ergodic with respect to the distribution with density proportional to $e^{-\beta H_n^0(q, \mathbf{v})}$.
- Dimension-free stability. For a harmonically confined ring polymer [i.e., for $V(q) = (\Lambda/2) q^2$], the integrator with $y_{j,n} = 0$ is stable for any *n* if Δt leads to stable integration for n = 1.
- (P4) Dimension-free ergodicity. For a harmonically confined ring polymer, the integrator with $y_{i,n} > 0$ is ergodic with respect to its stationary distribution for any n.
- Dimension-free equilibrium accuracy. For a harmonically confined ring polymer, the integrator leaves invariant an accurate approximation of the distribution with density proportional to $e^{-\frac{\beta m_n}{2}q^{\mathrm{T}}(\frac{\Lambda}{m}+\Omega^2)q}$, with bounded error for any n.

To obtain integrators satisfying properties (P1)-(P5), we introduce a function θ that defines the free ring-polymer update and then construct θ accordingly. To this end, let

$$S_{j,n}^{1/2} = \mathcal{Q}_{j,n} \begin{bmatrix} e^{i\theta(\omega_{j,n}\Delta t)/2} & 0\\ 0 & e^{-i\theta(\omega_{j,n}\Delta t)/2} \end{bmatrix} \mathcal{Q}_{j,n}^{-1}, \tag{11}$$

where $\mathcal{Q}_{j,n} = \begin{bmatrix} 1 & 1 \\ i\omega_{j,n} & -i\omega_{j,n} \end{bmatrix}$, and essential properties of θ are determined in the sequel. We focus on T-RPMD schemes derived from the BAOAB splitting [i.e., a = 0 in Eq. (10)] with the exact free ringpolymer update replaced by $S_{in}^{1/2}$. For such schemes, an integration time step is comprised by the following sequence of sub-steps:

Update velocities for half a step: $\mathbf{v} \leftarrow \mathbf{v} + \frac{\Delta t}{2} \frac{F}{m_n}$. Convert bead Cartesian coordinates to normal modes using

$$\rho = \boldsymbol{U}^{\mathrm{T}} \boldsymbol{q}$$
 and $\boldsymbol{\varphi} = \boldsymbol{U}^{\mathrm{T}} \boldsymbol{v}$. (12)

A: Evolve the free ring polymer in normal-mode coordinates for half a step:

$$\begin{bmatrix} Q_j \\ \varphi_j \end{bmatrix} \leftarrow \mathcal{S}_{j,n}^{1/2} \begin{bmatrix} Q_j \\ \varphi_j \end{bmatrix} \quad \text{for } 0 \le j \le n-1.$$

O: Perform an Ornstein-Uhlenbeck velocity update for a full time step:

$$\varphi_j \leftarrow e^{-\gamma_{j,n}\Delta t} \varphi_j + \sqrt{\frac{1 - e^{-2\gamma_{j,n}\Delta t}}{\beta m_n}} \xi_j,$$

where ξ_i are independent standard normal random variables and $0 \le j \le n - 1$.

Evolve the free ring polymer in normal-mode coordinates for half a step:

$$\begin{bmatrix} Q_j \\ \varphi_j \end{bmatrix} \leftarrow \mathcal{S}_{j,n}^{1/2} \begin{bmatrix} Q_j \\ \varphi_j \end{bmatrix} \quad \text{for } 0 \le j \le n-1.$$

Convert back to bead Cartesian coordinates using the inverse of U, which is just its transpose since U is orthogonal.

B: Update velocities for half a step: $\mathbf{v} \leftarrow \mathbf{v} + \frac{\Delta t}{2} \frac{F}{m_n}$.

In the remainder of this section, we identify conditions on the choice of θ that imply properties (P1)-(P5) for the corresponding T-RPMD integrator. Despite our focus on BAOABlike splittings, we describe how the conditions on θ can be adjusted to construct integrators derived from the OBABO splitting [i.e., a = 1 in Eq. (10)], which satisfy properties (P1)-(P5).

B. Strong stability of RPMD with a constant external potential

In this section, sufficient conditions on θ are identified to satisfy property (**P1**) in Sec. II A. Let V(q) = const. and $y_{i,n} = 0$ for $1 \le j$ $\leq n-1$, corresponding to the free ring polymer. The jth normal mode $[\varrho_i \ \varphi_i]^T$ satisfies

$$\begin{bmatrix} \dot{Q}_j \\ \dot{\varphi}_j \end{bmatrix} = \mathbf{A}_{j,n} \begin{bmatrix} Q_j \\ \varphi_j \end{bmatrix}, \quad \text{where} \quad \mathbf{A}_{j,n} = \begin{bmatrix} 0 & 1 \\ -\omega_{j,n}^2 & 0 \end{bmatrix}. \tag{13}$$

In this case, the algorithm from Sec. II A reduces to a full step of $S_{j,n} \approx \exp(\Delta t A_{j,n})$, i.e.,

$$\begin{bmatrix} \varrho_j \\ \varphi_j \end{bmatrix} \leftarrow \mathcal{S}_{j,n} \begin{bmatrix} \varrho_j \\ \varphi_j \end{bmatrix} \quad \text{for } 0 \le j \le n-1, \tag{14}$$

where $S_{j,n} = S_{j,n}^{1/2} S_{j,n}^{1/2}$ follows from Eq. (11), and the function θ is such that property (P1) holds.

We proceed to identify sufficient conditions on θ such that the corresponding free ring-polymer update satisfies property (P1).

First, note that for any function θ such that $\theta(-x) = -\theta(x)$ for x > 0, the structure of $S_{j,n}^{1/2}$ guarantees that the corresponding free ring-polymer update is reversible, symplectic, and preserves the free ring-polymer Hamiltonian $H_n^0(\mathbf{q}, \mathbf{v})$. Now, observe that $S_{j,n}$ is exact if $\theta(x) = x$; therefore, second-order accuracy requires that θ approximates the identity near the origin, i.e.,

$$\theta(0) = 0, \ \theta'(0) = 1, \ \text{and} \ \theta''(0) = 0.$$
 (S1a)

Moreover, strong stability follows if the eigenvalues $e^{\pm i\theta(\omega_{j,n}\Delta t)}$ of $S_{j,n}$ are distinct;⁴¹ to this end, we require that

$$0 < \theta(x) < \pi \quad \text{for } x > 0. \tag{S2a}$$

Jointly, conditions (S1a) and (S2a) guarantee that the update in Eq. (14) satisfies property (P1). There are many different choices of θ that obey these conditions, e.g., $\theta(x) = \arctan(x)$, $\arccos(\operatorname{sech}(x))$, and 2 $\arctan(x/2)$. The latter choice leads to the Cayley approximation of the free ring-polymer update, as can be verified by substitution in Eq. (11) and comparison of the resulting $\mathcal{S}_{j,n}^{1/2}$ with Eq. (17) in Ref. 43. Figure 1 compares the eigenvalues of $\mathcal{S}_{j,n}$ with $\theta(x) = x$ and several choices of θ that meet conditions (S1a) and (S2a).

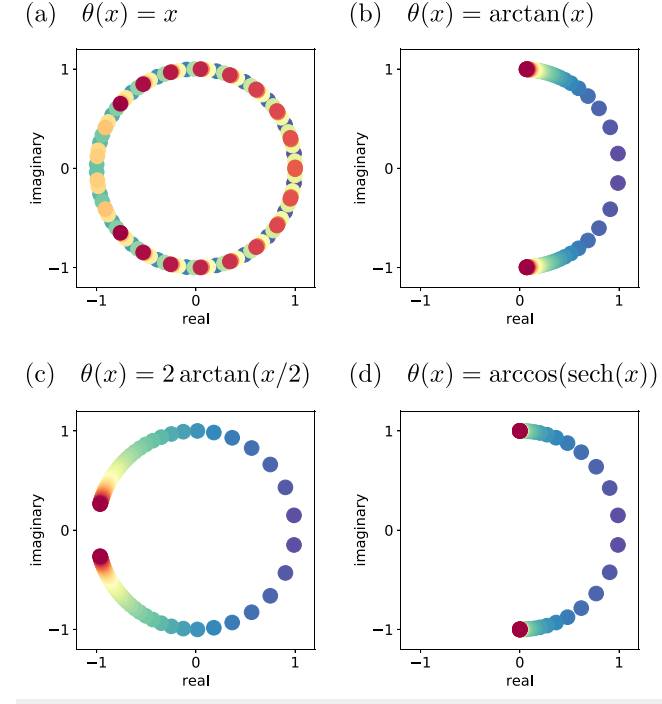


FIG. 1. Eigenvalues of $\mathcal{S}_{j,n}$ for 50 different time step sizes between 0.05 and 5.0 (evenly spaced) and fixed Matsubara frequency $\omega = 3$. The colors go from blue (smallest time step) to green and yellow to red (largest time step). In panel (a), the eigenvalues rotate around the unit circle several times, which indicates that the corresponding $\mathcal{S}_{j,n}$ is not always strongly stable. In panels (b)–(d), the eigenvalues are distinct and on the unit circle; thus, the corresponding $\mathcal{S}_{i,n}$ is strongly stable.

C. Ergodicity of T-RPMD with a constant external potential

In this section, it is shown that condition (S2a) implies property (**P2**) in Sec. II A. Let V(q) = const. and $y_{j,n} > 0$ for $1 \le j \le n-1$, corresponding to the free ring polymer with an Ornstein–Uhlenbeck thermostat. In this case, the jth normal mode satisfies

$$\begin{bmatrix} \dot{Q}_j \\ \dot{\varphi}_j \end{bmatrix} = (\mathbf{A}_{j,n} + \mathbf{C}_{j,n}) \begin{bmatrix} Q_j \\ \varphi_j \end{bmatrix} + \begin{bmatrix} 0 \\ \sqrt{\frac{2\gamma_{j,n}}{\beta m_n}} \dot{W}_j \end{bmatrix}, \tag{15}$$

where $C_{j,n} = \begin{bmatrix} 0 & 0 \\ 0 & -\gamma_{j,n} \end{bmatrix}$ and \dot{W}_j is a scalar white-noise. The solution

 $\left[\varrho_{j}(t)\ \varphi_{j}(t)\right]^{\mathrm{T}}$ of Eq. (15) is an ergodic Markov process, and in the limit as $t\to\infty$, its distribution converges to the centered bivariate normal with covariance

$$\Sigma_{j,n} = \frac{1}{\beta m_n} \begin{bmatrix} s_{j,n}^2 & 0 \\ 0 & 1 \end{bmatrix}, \text{ where } s_{j,n}^2 = \frac{1}{\omega_{j,n}^2}.$$
 (16)

This distribution corresponds to the *j*th marginal of the free ring-polymer equilibrium distribution with density proportional to $_{\rho}^{-\beta H_{\eta}^{0}(q,v)}$

The choice of $\gamma_{j,n} > 0$ in Eq. (15) determines the rate at which the associated Markov process converges to its stationary distribution if initialized away from it. When $\gamma_{j,n} < 2\omega_{j,n}$, the process is dominated by the deterministic Hamiltonian dynamics and is characterized as *underdamped*; on the other hand, when $\gamma_{j,n} > 2\omega_{j,n}$, the process is *overdamped*; and at the critical value $\gamma_{j,n} = 2\omega_{j,n}$, the process is characterized as *critically damped* and converges to equilibrium fastest. This analytical result motivates the so-called PILE friction schedule. We specialize to this schedule in the remainder of the section and set $\gamma_{j,n} = 2\omega_{j,n}$ for $1 \le j \le n - 1$.

The BAOAB-like update in Sec. II A applied to Eq. (15) can be written compactly as

$$\begin{bmatrix} Q_j \\ \varphi_j \end{bmatrix} \leftarrow \mathcal{M}_{j,n} \begin{bmatrix} Q_j \\ \varphi_j \end{bmatrix} + \mathcal{R}_{j,n}^{1/2} \begin{bmatrix} \xi_j \\ \eta_j \end{bmatrix} \quad \text{for } 0 \le j \le n-1, \tag{17}$$

where ξ_j and η_j are independent standard normal random variables, and we have introduced the 2 × 2 matrices

$$\mathcal{M}_{j,n} = \mathcal{S}_{j,n}^{1/2} \mathcal{O}_{j,n} \mathcal{S}_{j,n}^{1/2}, \quad \mathcal{O}_{j,n} = \begin{bmatrix} 1 & 0 \\ 0 & e^{-2\omega_{j,n}\Delta t} \end{bmatrix},$$

and

$$\boldsymbol{\mathcal{R}}_{j,n} \ = \ \frac{1 - e^{-4\omega_{j,n}\Delta t}}{\beta m_n} \boldsymbol{\mathcal{S}}_{j,n}^{1/2} \begin{bmatrix} 0 & 0 \\ 0 & 1 \end{bmatrix} (\boldsymbol{\mathcal{S}}_{j,n}^{1/2})^{\mathrm{T}}.$$

Since $S_{j,n}^{1/2}$ and the Ornstein–Uhlenbeck update are individually preservative irrespective of the chosen θ , Eq. (17) exactly preserves the free ring-polymer equilibrium distribution for any choice of θ that satisfies (S1a) and (S2a).

The ergodicity of the integrator specified by Eq. (17) depends entirely on the asymptotic stability of $\mathcal{M}_{j,n}$, i.e., whether or not $\|\mathcal{M}_{j,n}^k\| \to 0$ as $k \to \infty$ where $\|\cdot\|$ is a matrix norm. The matrix $\mathcal{M}_{j,n}$ is asymptotically stable if its *spectral radius* (i.e., the modulus of its largest eigenvalue) is smaller than unity, 32 which depends on

$$\det(\mathcal{M}_{i,n}) = e^{-2\omega_{j,n}\Delta t}$$

and

$$\operatorname{tr}(\mathcal{M}_{j,n}) = \cos(\theta(\omega_{j,n}\Delta t))(1 + e^{-2\omega_{j,n}\Delta t}).$$

In particular, the eigenvalues of $\mathcal{M}_{j,n}$ are both inside the unit circle if and only if

$$|\operatorname{tr}(\mathcal{M}_{j,n})| < 1 + \operatorname{det}(\mathcal{M}_{j,n}) < 2,$$

and a proof of this claim is provided in Appendix A. This inequality reveals that condition (S2a) implies property (P2). Moreover, if $\operatorname{tr}(\mathcal{M}_{j,n})^2 - 4 \operatorname{det}(\mathcal{M}_{j,n}) \leq 0$, then the spectral radius of $\mathcal{M}_{j,n}$ is minimal and equal to $\sqrt{\det(\mathcal{M}_{j,n})} = e^{-\omega_{j,n}\Delta t}$; this occurs when $|\cos(\theta(\omega_{j,n}\Delta t))| \leq \operatorname{sech}(\omega_{j,n}\Delta t)$ for all $\omega_{j,n}\Delta t$, which holds if the

$$\arccos(\operatorname{sech}(x)) \le \theta(x) \le \pi - \arccos(\operatorname{sech}(x))$$
 for $x > 0$. (18)

Any choice of θ that does not satisfy Eq. (18) will be overdamped in some modes, in the sense that the corresponding $\mathcal{M}_{j,n}$ will have a spectral radius strictly larger than $e^{-\omega_{j,n}\Delta t}$.

The function $\theta(x) = \arccos(\operatorname{sech}(x))$ saturates the (left) inequality in Eq. (18) while satisfying conditions (S1a) and (S2a) and hence provides a strongly stable and critically damped integrator for the thermostatted free ring polymer. As illustration of this, Fig. 2(a) shows that $\theta(x) = \arctan(x)$ is overdamped for all modes, whereas the Cayley angle $\theta(x) = 2\arctan(x/2)$ exhibits mixed damping. In contrast, the function $\theta(x) = \arccos(\operatorname{sech}(x))$ preserves the critically damped behavior of its continuous counterpart under the PILE friction schedule. Figure 2(b) confirms that the spectral radius of $\mathcal{M}_{j,n}$ is minimal at $\theta(x) = \arccos(\operatorname{sech}(x))$ for x > 0; consequently, this choice of θ optimizes the convergence of the integrator to stationarity.

Conditions (S1a) and (S2a) also imply property (P2) for the OBABO-like update associated with a compliant choice of θ because the matrices $S_{j,n}^{1/2} \mathcal{O}_{j,n} S_{j,n}^{1/2}$ and $\mathcal{O}_{j,n}^{1/2} S_{j,n} \mathcal{O}_{j,n}^{1/2}$ have equal spectral

D. Dimension-free stability of RPMD with a harmonic external potential

In this section, we identify a condition on θ that yields property (P3) in Sec. II A. Let $V(q) = (\Lambda/2) q^2$ and $\gamma_{j,n} = 0$ for $1 \le j \le n-1$, corresponding to the non-thermostatted ring polymer with a harmonic external potential. In this case, the *j*th normal mode satisfies

$$\begin{bmatrix} \dot{Q}_j \\ \dot{\varphi}_j \end{bmatrix} = (\mathbf{A}_{j,n} + \mathbf{B}) \begin{bmatrix} Q_j \\ \varphi_j \end{bmatrix}, \tag{19}$$

where $\mathbf{B} = \begin{bmatrix} 0 & 0 \\ -\Lambda/m & 0 \end{bmatrix}$, and conserves the Hamiltonian

$$H_{j,n}(\rho_j,\varphi_j) = \frac{m_n}{2} (|\varphi_j|^2 + (\omega_{j,n}^2 + \Lambda/m)|\varrho_j|^2).$$

For this system, the BAOAB-like update in Sec. II A reduces to

$$\begin{bmatrix} Q_j \\ \varphi_j \end{bmatrix} \leftarrow \mathcal{M}_{j,n} \begin{bmatrix} Q_j \\ \varphi_j \end{bmatrix} \quad \text{for } 0 \le j \le n-1, \tag{20}$$

where we have introduced the 2×2 matrices.

$$\mathcal{M}_{j,n} = \mathcal{B}^{1/2} \mathcal{S}_{j,n} \mathcal{B}^{1/2} \text{ and } \mathcal{B}^{1/2} = \begin{bmatrix} 1 & 0 \\ -\Delta t (\Lambda/m)/2 & 1 \end{bmatrix}$$

This update may be interpreted as a symplectic perturbation of the free ring-polymer update in Eq. (14) due to the harmonic external potential⁴¹ and conserves a modification of $H_{i,n}$ that depends on the choices of θ and Δt .⁵¹

The update in Eq. (20) is stable if³⁴

$$\max_{0 \le j \le n-1} \frac{1}{2} |\operatorname{tr}(\mathcal{M}_{j,n})| = \max_{0 \le j \le n-1} |\mathcal{A}_{j,n}| < 1, \tag{21}$$

where

$$\mathcal{A}_{j,n} = \cos(\theta(\omega_{j,n}\Delta t)) - \frac{\Delta t^2(\Lambda/m)}{2} \frac{\sin(\theta(\omega_{j,n}\Delta t))}{\omega_{j,n}\Delta t}.$$

Moreover, the 0th (i.e., centroid) mode, like the single-bead ring polymer, evolves through the velocity Verlet algorithm, whose stability requires that $\Delta t^2 \Lambda/m < 4$. Combining this requirement with condition (S2a) yields a sufficient condition for Eq. (21) to hold at

$$0 < \theta(x) \le 2\arctan(x/2) \quad \text{for } x > 0.$$
 (S3a)

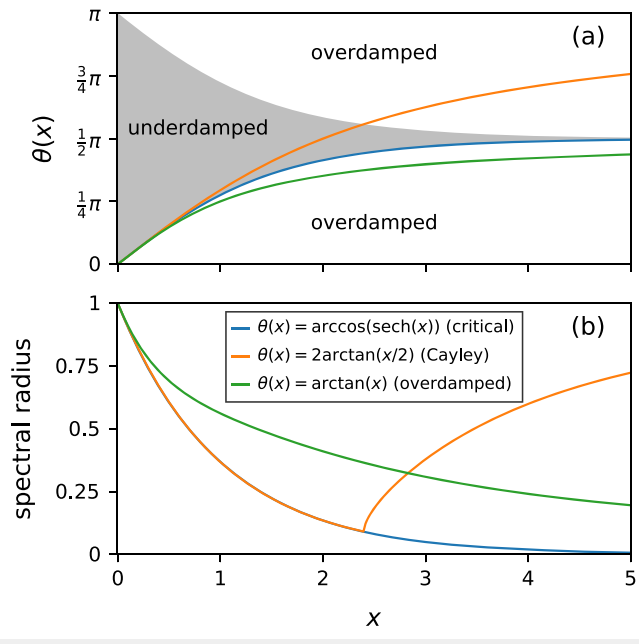


FIG. 2. Spectral properties of the T-RPMD update for the free ring polymer for various choices of θ . Panel (a) plots the functions $\theta(x) = \arccos(\operatorname{sech}(x))$, arctan(x), and arctan(x/2), and regions of overdamping and underdamping with PILE friction, separated at the locus of points where $|\cos(\theta(x))\cosh(x)| = 1$. The gray region $[|\cos(\theta(x))\cosh(x)| < 1]$ is where the dynamics is underdamped, while in the white region $[|\cos(\theta(x)) \cosh(x)| > 1]$, the dynamics is overdamped. The function $\theta(x)$ = arctan(x) lies in the overdamped region for x > 0, whereas $\theta(x) = 2 \arctan(x/2)$ is in the underdamped region for $x \lesssim 2.4$ and in the overdamped region otherwise. The function $\theta(x) = \arccos(\operatorname{sech}(x))$, however, is critically damped for x > 0 and optimizes the convergence rate of the integrator. Panel (b) plots the spectral radius of $\mathcal{M}_{i,n}$ corresponding to each choice of θ .

A proof of this result is provided in Appendix B. The functions $\theta(x)$ = $2 \arctan(x/2)$, $\arctan(x)$, and $\arccos(\operatorname{sech}(x))$ all satisfy condition (S3a), which ensures that the corresponding RPMD integrator meets property (P3).

E. Dimension-free ergodicity and equilibrium accuracy of T-RPMD with a harmonic external potential

In this section, it is shown that condition (S3a) implies property (P4) in Sec. II A, and an additional condition is introduced to ensure that property (**P5**) holds. Let $V(q) = (\Lambda/2) q^2$ and $\gamma_{j,n} = 2\omega_{j,n}$ for $1 \le 1$ $j \le n - 1$. In this case, the *j*th normal mode satisfies

$$\begin{bmatrix} \dot{Q}_j \\ \dot{\varphi}_j \end{bmatrix} = (\mathbf{A}_{j,n} + \mathbf{B} + \mathbf{C}_{j,n}) \begin{bmatrix} \varrho_j \\ \varphi_j \end{bmatrix} + \begin{bmatrix} 0 \\ \sqrt{\frac{4\omega_{j,n}}{\beta m_n}} \dot{W}_j \end{bmatrix}. \tag{22}$$

The solution $[\varrho_j(t) \ \varphi_j(t)]^T$ of Eq. (22) is an ergodic Markov process, and its distribution as $t \to \infty$ converges to the centered bivariate normal with the covariance matrix

$$\Sigma_{j,n} = \frac{1}{\beta m_n} \begin{bmatrix} s_{j,n}^2 & 0\\ 0 & 1 \end{bmatrix}, \text{ where } s_{j,n}^2 = \frac{1}{\Lambda/m + \omega_{j,n}^2};$$
 (23)

the associated position-marginal is the jth marginal of the ringpolymer configurational distribution with density $e^{-\frac{\beta m_n}{2}q^{\mathrm{T}}\left(\frac{\Lambda}{m}+\Omega^2\right)q}$.

For this system, the BAOAB-like update in Sec. II A is of the same form as Eq. (17) with

$$\mathcal{M}_{j,n} = \mathcal{B}^{1/2} \mathcal{S}_{j,n}^{1/2} \mathcal{O}_{j,n} \mathcal{S}_{j,n}^{1/2} \mathcal{B}^{1/2} \quad \text{and}$$

$$\mathcal{R}_{j,n} = \frac{1 - e^{-4\omega_{j,n}\Delta t}}{\beta m_n} \mathcal{B}^{1/2} \mathcal{S}_{j,n}^{1/2} \begin{bmatrix} 0 & 0 \\ 0 & 1 \end{bmatrix} (\mathcal{B}^{1/2} \mathcal{S}_{j,n}^{1/2})^{\mathrm{T}}. \tag{24}$$

As in the case of a constant external potential (see Sec. II C), the ergodicity of this integrator depends on the spectral radius of $\mathcal{M}_{i,n}$. By Theorem 1 in Appendix A and the fact that

$$\det(\mathcal{M}_{j,n}) = e^{-2\omega_{j,n}\Delta t}$$

and

$$\operatorname{tr}(\mathcal{M}_{i,n}) = \mathcal{A}_{i,n}(1 + e^{-2\omega_{j,n}\Delta t}),$$

it follows that condition (S3a) gives a simple and sufficient condition for ergodicity at any bead number *n* and hence implies property (P4) for the BAOAB-like update specified by Eqs. (17) and (24). Furthermore, because the matrix $\mathcal{M}_{j,n}$ of the corresponding OBABOlike update has equal trace and determinant, condition (S3a) also guarantees property (P4) in that case.

If condition (S3a) holds, the BAOAB-like update is ergodic with respect to a centered bivariate normal distribution whose covariance matrix $\Sigma_{i,\Delta t}$ satisfies the linear equation

$$\Sigma_{j,\Delta t} = \mathcal{M}_{j,n} \Sigma_{j,\Delta t} \mathcal{M}_{j,n}^{\mathrm{T}} + \mathcal{R}_{j,n}, \tag{25}$$

for which the solution is

$$\Sigma_{j,\Delta t} = \frac{1}{\beta m_n} \begin{bmatrix} s_{j,\Delta t}^2 & 0\\ 0 & r_{j,\Delta t}^2 \end{bmatrix},\tag{26}$$

where the variance in the position- and velocity-marginal is $(\beta m_n)^{-1} s_{i,\Delta t}^2$ and $(\beta m_n)^{-1} r_{i,\Delta t}^2$, respectively, with

$$s_{j,\Delta t}^{2} = \left(\omega_{j,n}^{2} + \frac{\Lambda}{m} \frac{\omega_{j,n} \Delta t/2}{\tan(\theta(\omega_{j,n} \Delta t)/2)}\right)^{-1} \quad \text{and}$$

$$r_{j,\Delta t}^{2} = 1 - \frac{\Delta t^{2} \Lambda}{4 m} \frac{\tan(\theta(\omega_{j,n} \Delta t)/2)}{\omega_{j,n} \Delta t/2}.$$
(27)

Because the tangent function is monotonically increasing on the range of θ specified by condition (S3a), we have the correspondence

$$0 < s_{j,\Delta t}^2 \le s_j^2 \quad \text{and} \quad 1 - \frac{\Delta t^2 \Lambda}{4 m} \le r_{j,\Delta t}^2 < 1$$
 (28)

between the exact and numerical variances of the jth ring-polymer mode. Equation (27) reveals that $\theta(x) = 2 \arctan(x/2)$ is the unique function that complies with condition (S3a) and saturates the inequality $s_{i,\Delta t}^2 \leq s_i^2$ in Eq. (28); consequently, the corresponding BAOAB-like scheme preserves the exact position-marginal in all modes and trivially satisfies property (P5). The BCOCB integrator from Ref. 43 corresponds to this choice of θ and, thus, uniquely provides optimal equilibrium position-marginal accuracy for harmonic external potentials.

To identify other BAOAB-like schemes compliant with condition (S3a), which satisfy property (P5), we examine the overlap between the numerical stationary position-marginal distribution $\mu_{n,\Delta t}$ and the exact distribution μ_n where

$$\mu_n = \prod_{j=1}^{n-1} \mathcal{N}\left(0, \frac{s_j^2}{\beta m_n}\right) \quad \text{and} \quad \mu_{n,\Delta t} = \prod_{j=1}^{n-1} \mathcal{N}\left(0, \frac{s_{j,\Delta t}^2}{\beta m_n}\right).$$

Centroid-mode marginals have been suppressed in the definitions of μ_n and $\mu_{n,\Delta t}$. A BAOAB-like scheme is dimension-free if it admits an *n*-independent upper bound on the distance $d_{\text{TV}}(\mu_n, \mu_{n,\Delta t})$ between μ_n and $\mu_{n,\Delta t}$, where $d_{\rm TV}$ is the total variation metric.⁵³ In particular, if we require

$$\frac{x}{1+|x|} \le \theta(x) \le 2\arctan(x/2) \quad \text{for } x > 0,$$
 (S4a)

then we have the dimension-free bound

$$d_{\text{TV}}(\mu_n, \mu_{n,\Delta t}) < \left(\sqrt{\frac{4}{3}} \frac{\hbar \beta}{\Delta t}\right) \frac{\Delta t^2 \Lambda}{m}.$$
 (29)

A proof of this claim is provided in Appendix D. Condition (S4a) ensures that any BAOAB-like integrator with a compliant choice of θ meets property (P5).

For OBABO-like schemes, the bound in condition (S4a) must be tightened to guarantee non-zero overlap between μ_n and $\mu_{n,\Delta t}$ for arbitrarily large n. In particular, replacing $2\arctan(x/2)$ with $\min\{2\arctan(x/2), C\}$ for some $C \in (0, \pi)$ in the upper bound of condition (S4a) yields a *n*-independent bound on $d_{\text{TV}}(\mu_n, \mu_{n,\Delta t})$ for all compliant OBABO-like integrators, as can be shown through arguments similar to those in Appendix D.

Jointly, conditions (S1a)-(S4a) specify a family of BAOAB-like schemes with dimension-free stability, ergodicity, and equilibrium accuracy for applications with harmonic external potentials. Numerical results in Sec. III suggest that the integrators exhibit similar properties in a more realistic setting with a strongly anharmonic external potential.

F. Dimension-free convergence to equilibrium of T-RPMD with a harmonic external potential

Beyond ensuring ergodicity of the T-RPMD update in Eq. (24), condition (S3a) leads to explicit dimension-free equilibration rates for compliant schemes. Theorem 4 in Appendix C proves this result in the infinite-friction limit for ring-polymer modes with arbitrarily high frequency. In detail, the theorem shows that the configurational (i.e., position-marginal) transition kernel associated with the T-RPMD update of the jth mode in Eq. (24) is contractive in the 2-Wasserstein metric⁵⁴ and equilibrates any given initial distribution at a rate determined by the function θ , the (external) potential curvature Λ , and the (stable) time step Δt if condition (S3a) holds. The rate in Theorem 4 in Appendix C, though obtained in the infinite-friction limit, holds for finite friction coefficients $y_{j,n}$ that lead to spectral radii $\rho(\mathcal{M}_{j,n}) \leq |\mathcal{A}_{j,n}|$, where $\mathcal{A}_{j,n}$ is defined in the display after Eq. (21) and $|\mathcal{A}_{j,n}| = \lim_{\gamma_{j,n} \to \infty} \rho(\mathcal{M}_{j,n})$ is the spectral radius at infinite friction.

To illustrate dimension-free convergence, Fig. 3 plots the 2-Wasserstein distance between the stationary configurational distribution $\mu_{n,\Delta t}$ and the distribution $\mu_{n,\Delta t}^k$ at the kth T-RPMD step evolved from a point mass at the origin using the schemes specified by $\theta(x) = \arccos(\operatorname{sech}(x))$ [Fig. 3(a)], $2\arctan(x/2)$ [Fig. 3(b)], and $\arctan(x)$ [Fig. 3(c)] for a range of bead numbers n. These choices of θ , respectively, lead to *overdamped*, *critical*, and *Cayley* evolution of the thermostatted free ring polymer under PILE friction (see Sec. II C) and are identified accordingly in Fig. 3. The ring-polymer system considered in Fig. 3 approximates the O-H stretch dynamics in liquid water at room temperature with the parameters listed in Sec. III A. Velocity-marginals were initialized as in the setting of Theorem 4 (see Appendix C), and the position of the jth ring-polymer mode at time $k\Delta t$ follows a centered normal distribution with variance $(\beta m_n)^{-1}(s_{i\Delta t}^k)^2$, where

$$\left(s_{j,\Delta t}^{k}\right)^{2} = \left(\boldsymbol{\mathcal{M}}_{j,n}^{k}\right)_{12}^{2} + \beta m_{n} \sum_{\ell=0}^{k-1} \left(\boldsymbol{\mathcal{M}}_{j,n}^{\ell} \boldsymbol{\mathcal{R}}_{j,n} (\boldsymbol{\mathcal{M}}_{j,n}^{\ell})^{\mathrm{T}}\right)_{11} \quad \text{for } k > 0.$$

The 2-Wasserstein distances in Fig. 3 were evaluated using a well-known analytical result for multivariate normal distributions. ⁵⁵

Figures 3(a) and 3(c) clearly show that the critical and over-damped schemes converge at dimension-free rates, but this is less evident from Fig. 3(b) for the Cayley scheme. The latter scheme nonetheless displays an n-independent, and hence dimension-free, distance to stationarity at all times $k\Delta t > 0$, indicated by plateauing of the contour lines toward the right of Fig. 3(b). The ladder-like pattern that precedes this plateau illustrates a transition from geometric (i.e., fast) to sub-geometric (i.e., slow) convergence upon introducing higher-frequency modes into the ring polymer. The transition manifests with the Cayley scheme because of its aggressive overdamping of the high-frequency modes, which is absent in the other two schemes (see Fig. 2).

The example considered in this section illustrates that the equilibration timescale (e.g., the time until the 2-Wasserstein distance decays below 10^{-6}) of the Cayley scheme at large n can dramatically exceed that of other BAOAB-like schemes. Although this negative feature may render the scheme impractical for pathological applications, we find in Sec. III that the Cayley scheme's superior

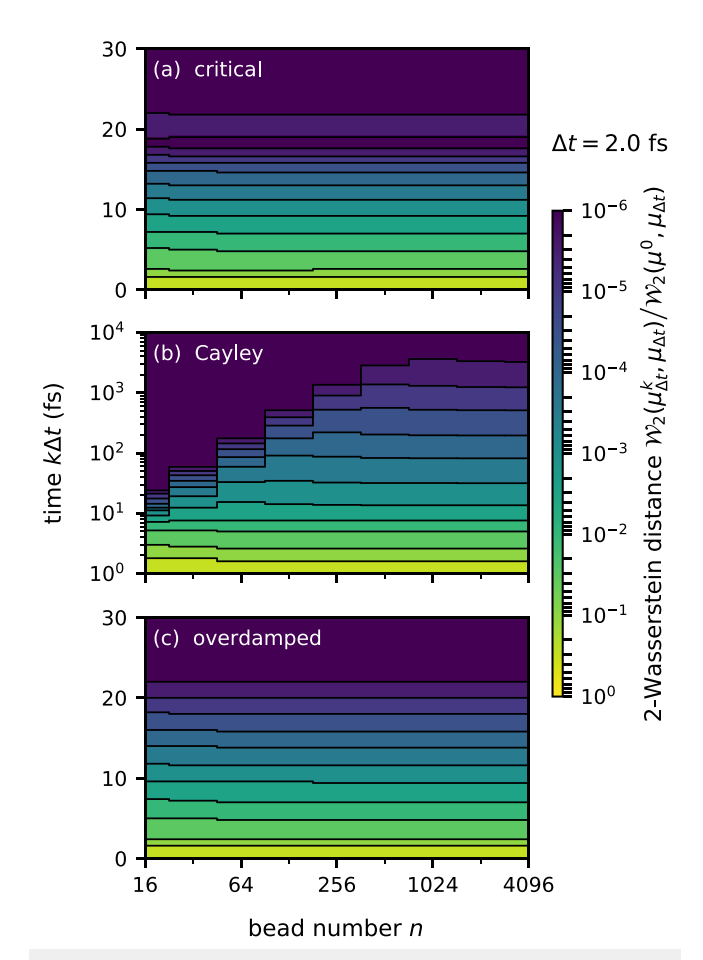


FIG. 3. Dimension-free convergence to equilibrium of BAOAB-like T-RPMD schemes with a harmonic external potential. The physical parameters of the ring-polymer system (i.e., Λ , m, and β) are listed in Sec. III A. Panels (a)–(c) plot the normalized 2-Wasserstein distance between the configurational ring-polymer distribution at stationarity and at time $k\Delta t$, as evolved via various BAOAB-like schemes from an initial point-mass distribution. Regions with darker color indicate the smaller 2-Wasserstein distance to stationarity, and black lines mark the iso-distance contours. The contours plateau at some value of n for all tested schemes, which checks that they exhibit dimension-free convergence, as predicted by Theorem 4 in Appendix C.

configurational sampling provides compelling justification for its preferred use in realistic settings.

III. NUMERICAL RESULTS

The current section provides numerical comparisons of the BAOAB-like T-RPMD integrators in Sec. II on applications featuring harmonic (Sec. III A) and anharmonic (Sec. III B) external potentials. Three representative choices of θ are considered in the numerical comparisons, namely, $\theta(x) = \arctan(x)$, $\arccos(\operatorname{sech}(x))$, and $2\arctan(x/2)$. These choices, respectively, lead to *overdamped*, *critical*, and *Cayley* evolution of the thermostatted free ring polymer under PILE friction (Sec. II C) and are identified accordingly throughout the current section. It is borne out from the numerical

comparisons that the Cayley scheme exhibits superior configurational sampling among the tested schemes in both applications.

A. One-dimensional quantum harmonic oscillator

In the current section, we numerically integrate Eq. (7) with the harmonic potential $V(q)=(\Lambda/2)~q^2$ using PILE friction (i.e., $\Gamma=2~\Omega$), m=0.95 amu, $\sqrt{\Lambda/m}=3886~{\rm cm}^{-1}$, and $T=298~{\rm K}$. This choice of physical parameters corresponds to a harmonic approximation of the Morse contribution to the O–H bond potential in the q-TIP4P/F force field for water ⁵⁶ and sets a least upper bound for the T-RPMD stability interval at $\Delta t^{\rm max}=2/\sqrt{\Lambda/m}=2.74~{\rm fs}$. The simulations reported throughout this section employ the time step $\Delta t=0.73\times\Delta t^{\rm max}=2.00~{\rm fs}$.

Figure 4 compares the accuracy and efficiency of various BAOAB-like T-RPMD schemes at equilibrium as a function of the

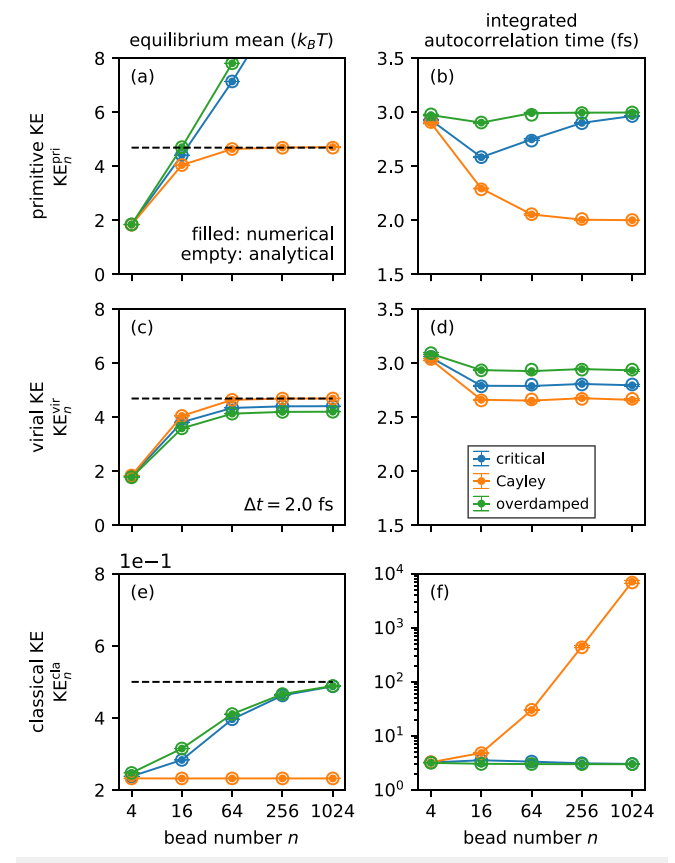


FIG. 4. Performance at equilibrium of various BAOAB-like T-RPMD schemes applied to the one-dimensional quantum harmonic oscillator with physical parameters listed in Sec. III A. Panels (a), (c), and (e), respectively, plot the equilibrium mean primitive kinetic energy, virial kinetic energy, and non-centroid classical kinetic energy per mode as a function of bead number n; the corresponding means in the exact infinite bead limit are plotted as dashed lines. Panels (b), (d), and (f) plot the integrated autocorrelation times [Eq. (31)] of the respective observables. Exact (respectively, numerically estimated) values of the plotted quantities are shown with empty (respectively, filled) circles. Numerical estimates were obtained using the protocol described in Appendix G.

bead number n. For a description of the numerical simulation and statistical estimation procedures used to generate the numerical data (filled circles) in Fig. 4, the reader is referred to Appendix G. Figures 4(a) and 4(c) report the mean quantum kinetic energy at equilibrium as per the primitive and virial estimators,

$$\mathsf{KE}_{n}^{\mathrm{pri}}(\boldsymbol{q}) = \frac{n}{2\beta} - \sum_{j=0}^{n-1} \frac{m_{n}\omega_{n}^{2}}{2} (q_{j+1} - q_{j})^{2} \quad \text{and}$$

$$\mathsf{KE}_{n}^{\mathrm{vir}}(\boldsymbol{q}) = \frac{1}{2\beta} + \frac{1}{2} \sum_{j=0}^{n-1} (q_{j} - \overline{q}) \partial_{q_{j}} V_{n}^{\mathrm{ext}}(\boldsymbol{q}), \tag{30}$$

where $\overline{q} = \frac{1}{n} \sum_{j=0}^{n-1} q_j$ is the centroid position of the *n*-bead ring polymer. For these two observables, Figs. 4(b) and 4(d) quantify the equilibrium sampling efficiency of the schemes in terms of the integrated autocorrelation time (or normalized asymptotic variance), ⁵⁷⁻⁶¹

$$\frac{\operatorname{aVar}(\mathsf{O}_{n})}{\operatorname{Var}(\mathsf{O}_{n})} = \frac{\lim_{K \to \infty} \operatorname{Var}\left(\frac{1}{\sqrt{K}} \sum_{k=0}^{K-1} \mathsf{O}_{n}(\boldsymbol{\xi}^{(k\Delta t)})\right)}{\operatorname{Var}(\mathsf{O}_{n})}$$

$$= 1 + 2 \sum_{k=1}^{\infty} \operatorname{Cor}\left(\mathsf{O}_{n}(\boldsymbol{\xi}^{(0)}), \mathsf{O}_{n}(\boldsymbol{\xi}^{(k\Delta t)})\right), \quad (31)$$

where O_n is an n-bead observable, $\{\boldsymbol{\xi}^{(k\Delta t)}\}_{k=0}^{\infty} = \{(\boldsymbol{q}^{(k\Delta t)}, \boldsymbol{v}^{(k\Delta t)})\}_{k=0}^{\infty}$ is the stationary T-RPMD trajectory, $\operatorname{Var}(O_n)$ is the variance of O_n at equilibrium, and $\operatorname{Cor}(O_n(\boldsymbol{\xi}^{(0)}), O_n(\boldsymbol{\xi}^{(k\Delta t)}))$ is the lag- $k\Delta t$ autocorrelation of O_n along the T-RPMD trajectory. The integrated autocorrelation time of O_n is interpreted as the timescale over which adjacent observations along an equilibrium trajectory become statistically uncorrelated and is hence a measure of the efficiency of a T-RPMD scheme at estimating the mean of O_n with respect to the numerically sampled equilibrium distribution. Figures A(a)-A(d) show that the scheme specified by the Cayley angle (orange) outperforms others in terms of both accuracy and efficiency at estimating the equilibrium average of the quantum kinetic energy observables.

From the perspective of configurational accuracy, the optimality of the Cayley angle displayed in Figs. 4(a) and 4(c) is not surprising in light of the findings in Sec. II E. Less expected are the results in Figs. 4(b) and 4(d), which suggest that the Cayley angle is also optimal from the standpoint of configurational sampling efficiency for the quantum kinetic energy observables in Eq. (30). Appendix E supports this conjecture with an analytical result for harmonic external potentials.

Figure 4(e) plots the mean classical kinetic energy at equilibrium, as computed from the non-centroid ring-polymer velocities,

$$\mathsf{KE}_n^{\mathsf{cla}}(\boldsymbol{v}) = \frac{m_n}{2(n-1)} \sum_{i=0}^{n-1} (v_j^2 - \overline{v}^2) \approx \frac{1}{2\beta},$$
 (32)

and Fig. 4(f) plots the corresponding integrated autocorrelation time, as given by Eq. (31). For this observable, the equilibrium accuracy and efficiency of the Cayley scheme are significantly worse than those of the others as n increases. This is a consequence of the strongly overdamped behavior of Cayley T-RPMD at high frequencies (see Fig. 2), for which the integrator's ergodicity degrades as its spectral radius approaches unity. Note that this shortcoming of the Cayley scheme presents no adverse implications to the equilibrium sampling of observables that exclusively depend on the ring-polymer configuration, as confirmed by Figs. 4(a)-4(d).

In summary, Fig. 4 establishes that the T-RPMD scheme specified by the Cayley angle provides optimally accurate and efficient configurational sampling at equilibrium. To exploit this remarkable feature in practice, the scheme must manifest rapid convergence to equilibrium when initialized away from it, as is necessary in most realistic applications of T-RPMD. Fortunately, Theorem 4 in Appendix C guarantees that any BAOAB-like scheme compliant with conditions (S1a)–(S4a) features a contractive configurational transition kernel for any number of ring-polymer beads, and Fig. 3 in Sec. II F illustrates this fact for the quantum harmonic oscillator considered in the current section.

B. Room-temperature liquid water

While theoretical analysis and numerical tests of BAOAB-like T-RPMD schemes in Secs. II and III A have focused on harmonic external potentials, the current section demonstrates that the resulting insights carry over to a realistic, strongly anharmonic model of room-temperature liquid water. Our test system is a periodic box containing 32 water molecules at a temperature of 298 K and a density of 0.998 g/cm³, with potential energy described by the q-TIP4P/F force field.⁵⁶ As in Sec. III A, we compare the performance of various BAOAB-like T-RPMD schemes for integrating the many-dimensional analog of Eq. (7) with PILE friction using the simulation time step $\Delta t = 1.4$ fs in all simulations. Numerical tests reported in Appendix F show that this value of Δt closely approximates the upper limit of the Verlet (i.e., n = 1) stability interval for q-TIP4P/F liquid water. In agreement with Sec. III A, the experiments reveal that among the tested T-RPMD schemes, the Cayley scheme offers superior configurational sampling. For details on the numerical simulation and statistical estimation procedures used to generate the data presented in this section, the reader is referred to

Figure 5 compares the equilibrium accuracy achieved by the tested schemes in terms of the quantum and classical kinetic energy per hydrogen atom [Figs. 5(a), 5(c), and 5(i)] and the intramolecular potential energy per water molecule [Figs. 5(e) and 5(g)]; also plotted are the respective integrated autocorrelation times as a function of bead number n. The kinetic energy estimates in Figs. 5(a) and 5(c)exhibit similar trends to those seen in Fig. 4 for the one-dimensional harmonic oscillator. In particular, the T-RPMD scheme specified by the Cayley angle outperforms others in terms of quantum kinetic energy accuracy as n increases, most outstandingly with a highly accurate primitive kinetic energy estimate despite the large time step employed. Still in close agreement with the harmonic oscillator results, Figs. 5(b) and 5(d) show that the Cayley scheme displays the shortest integrated autocorrelation time among the tested schemes for the quantum kinetic energy observables. Similar trends manifest in the intramolecular potential energy averages and their autocorrelation times [Figs. 5(e)-5(h)], where the Cayley scheme also achieves superior accuracy and efficiency. Finally, Figs. 5(i) and 5(j) confirm that the relative performance of the compared schemes in terms of velocity-marginal sampling is qualitatively consistent with the harmonic results. Taken together, the results in Fig. 5 suggest that the superiority of the Cayley scheme for configurational sampling, proven in the model setting of a harmonic external potential, is also reflected in realistic applications.

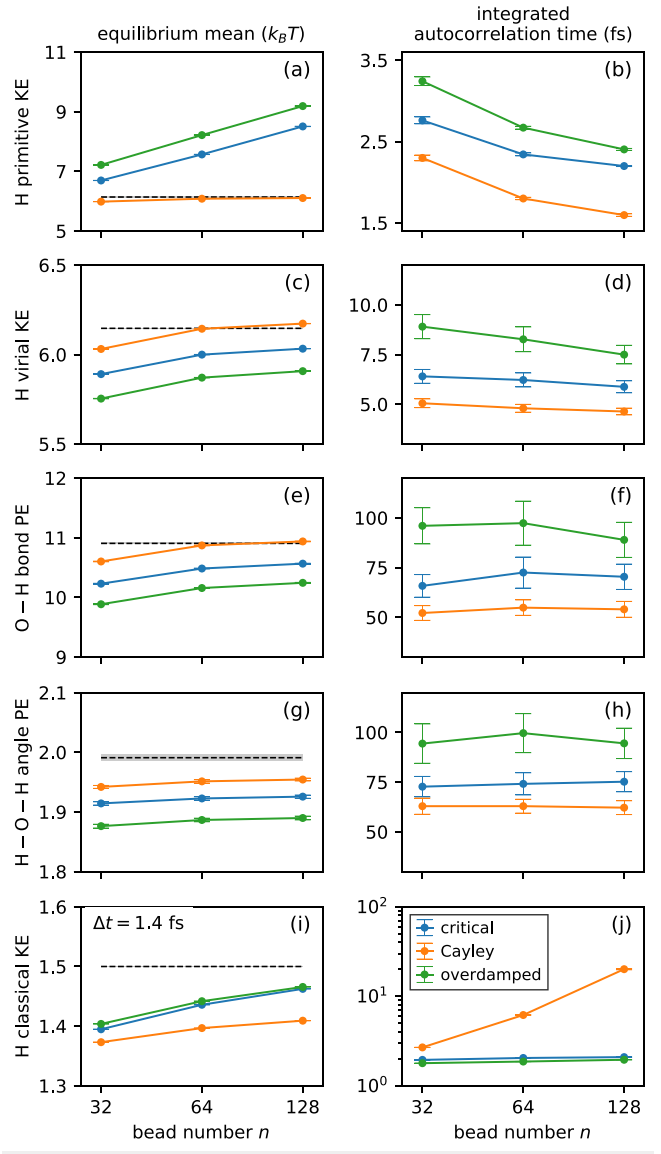


FIG. 5. Performance of various BAOAB-like T-RPMD schemes applied to q-TIP4P/F liquid water at room temperature. As a function of the bead number n and for a 1.4-fs time step, panels (a) and (c) plot the equilibrium kinetic energy per H atom as per the primitive and virial estimators [Eq. (30)], and panels (b) and (d) plot the corresponding integrated autocorrelation times. Likewise, panels (e) and (g) plot the equilibrium potential energy per H_2O molecule due to the O–H-stretch and H–O–H-bend contributions, as defined in the q-TIP4P/F force field, $\frac{1}{1}$ 6 and the corresponding autocorrelation times are plotted by panels (f) and (h). Finally, panel (i) plots the classical kinetic energy per H atom computed from the non-centroid velocity estimator [Eq. (32)], and panel (j) plots the corresponding autocorrelation time. The numerical estimates and reference results (dashed lines) were obtained using the protocols described in Appendix G.

In a final numerical test, Fig. 6 confirms that the sampling advantages of the Cayley T-RPMD scheme are obtained without downside in the estimation of dynamical quantities of typical interest. Specifically, Fig. 6(b) shows (unnormalized) infrared

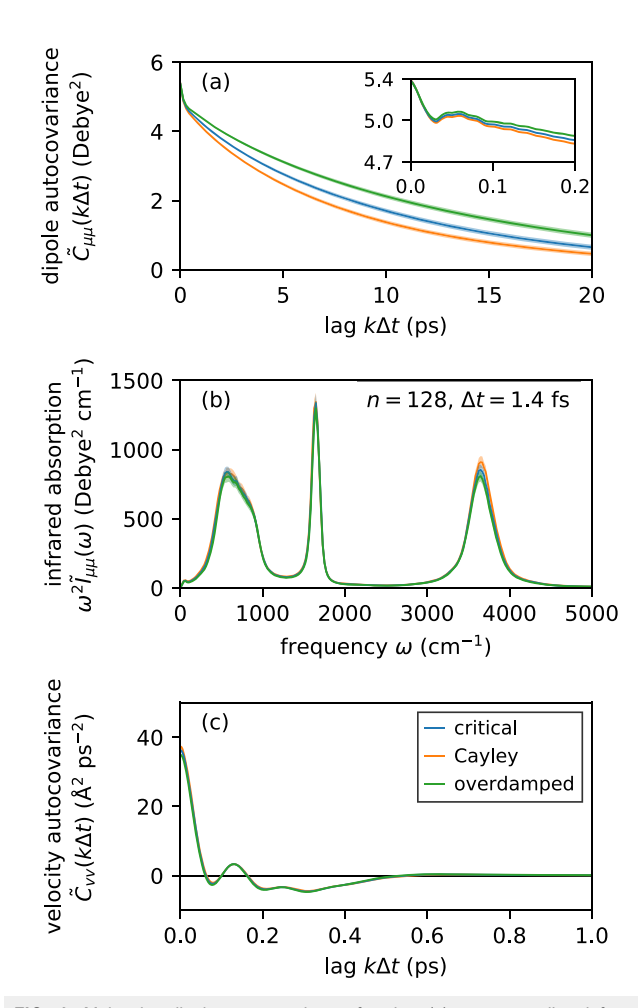


FIG. 6. Molecular dipole autocovariance function (a), corresponding infrared absorption spectrum (b), and molecular velocity autocovariance function (c) in room-temperature liquid water for various BAOAB-like T-RPMD schemes. The plotted autocovariance functions exhibit minor qualitative discrepancies across schemes, which suggests that all schemes compliant with conditions (S1a)–(S4a) exhibit comparable accuracy in the computation of dynamical properties. Numerical estimates of the autocovariance functions were obtained using the protocol described in Appendix G.

absorption spectra for room-temperature liquid water, computed from the 128-bead T-RPMD trajectories used to generate Fig. 5 using linear response theory and the T-RPMD approximation to real-time quantum dynamics. Linear response dictates that the absorption spectrum is proportional to $\omega^2 \tilde{\mathcal{I}}(\omega)$, where $\tilde{\mathcal{I}}(\omega) = \int_{\mathbb{R}} \mathrm{d}t \, e^{-i\omega t} \, \tilde{C}_{\mu\mu}(t)$ is the Fourier transform of the quantum-mechanical Kubotransformed dipole autocorrelation function $\tilde{C}_{\mu\mu}(t)$. The latter is approximated within the T-RPMD framework by $\tilde{C}_{\mu\mu}(t) \approx \frac{1}{N_{\mathrm{H}_2\mathrm{O}}} \sum_{i=1}^{N_{\mathrm{H}_2\mathrm{O}}} \mathbb{E}(\bar{\mu}_i(t) \cdot \bar{\mu}_i(0))$, where $N_{\mathrm{H}_2\mathrm{O}}$ is the number of molecules in the liquid, $\bar{\mu}_i(t)$ is the bead-averaged dipole moment of molecule i at time t, and the covariance $\mathbb{E}(\bar{\mu}_i(t) \cdot \bar{\mu}_i(0))$ is estimated from a stationary T-RPMD trajectory, as indicated in Appendix G. Figure 6(a) plots the T-RPMD estimates of $\tilde{C}_{\mu\mu}(t)$,

leading to the absorption spectra in Fig. 6(b). On the scale in which the absorption spectrum exhibits its key features, the spectra in Fig. 6(b) show very minor qualitative discrepancies. A similar conclusion holds for Fig. 6(c), where the T-RPMD approximation of the Kubo-transformed velocity autocovariance function $\tilde{C}_{vv}(t) \approx \frac{1}{N_{\rm H_2O}} \sum_{i=1}^{N_{\rm H_2O}} \mathbb{E}(\bar{v}_i(t) \cdot \bar{v}_i(0))$ is plotted for the three tested T-RPMD schemes. Collectively, these observations indicate that the accuracy of dynamical properties computed with BAOAB-like schemes is not significantly affected by the particular θ employed if conditions (S1a)–(S4a) in Sec. II are met. This result is expected due to the fact that the considered dynamical properties depend on bead-averaged (i.e., centroid-mode) coordinates, whose evolution is largely independent of the choice of θ under weak coupling between the centroid and non-centroid ring-polymer modes.

IV. SUMMARY

Previous studies showed that strong stability ⁴¹ and dimensionality freedom ⁴³ are essential features of a robust T-RPMD integration scheme that standard integrators do not possess. A T-RPMD scheme with these features, denoted by BCOCB, was introduced via a simple and inexpensive Cayley modification of the free ringpolymer update (i.e., the "A" sub-step) of the standard BAOAB integrator. The BCOCB scheme was then shown to dramatically outperform BAOAB at estimating static and dynamic properties of various systems with remarkable accuracy at unprecedented time steps. ⁴³

The current work generalizes beyond the Cayley modification by introducing a simple parameterization of the free ring-polymer update and a corresponding family of strongly stable and dimension-free modifications of the BAOAB scheme. Among these schemes lies BCOCB, which is found to exhibit superior configurational sampling despite exhibiting worse accuracy and efficiency for observables that depend on the non-centroid ring-polymer velocities. This conclusion is obtained theoretically via exhaustive analysis of a harmonic model and numerically via simulation of a realistic quantum-mechanical model of liquid water at room temperature. In this way, the current work convincingly demonstrates the superiority of the BCOCB scheme for accurate and efficient equilibrium simulation of condensed-phase systems with T-RPMD.

To conclude, we stress that implementing BCOCB or any of the new dimension-free and strongly stable schemes leads to no additional cost, parameters, or coding overhead relative to the standard BAOAB integrator. The modified integrators, thus, provide "turnkey" means to significantly improve the accuracy and stability of existing (T-)RPMD implementations. ^{62,63}

AUTHORS' CONTRIBUTIONS

J.L.R.-R. and J.S. contributed equally to this work.

ACKNOWLEDGMENTS

This work was supported in part by the U.S. Department of Energy (Grant No. DE-SC0019390) and the National Institutes of Health (Grant No. R01GM125063). N.B.-R. acknowledges support by the Alexander von Humboldt foundation and the National Science Foundation (Grant No. DMS-1816378).

APPENDIX A: NECESSARY AND SUFFICIENT CONDITION FOR EIGENVALUES OF A 2 × 2 REAL MATRIX TO BE INSIDE THE UNIT CIRCLE

This section provides a proof of the standard result used in Secs. II C and II E to infer ergodicity of the T-RPMD update for free and harmonically confined ring polymers.

Theorem 1. The spectral radius of a 2×2 real matrix M is strictly less than one if and only if

$$|\operatorname{tr}(\boldsymbol{M})| < 1 + \operatorname{det}(\boldsymbol{M}) < 2. \tag{A1}$$

Figure 7 plots eigenvalue pairs λ_1 , λ_2 that satisfy Eq. (A1) for a fixed value of $det(M) = \lambda_1 \lambda_2$. Note that the spectral radius of M is minimized when λ_1 and λ_2 are on the circle with radius $r = \sqrt{\det(\mathbf{M})}$.

Proof. Let λ_1 and λ_2 be the (possibly complex) eigenvalues of *M*. By definition, the spectral radius of *M* is max($|\lambda_1|, |\lambda_2|$) =: ρ . Since M is real, both $tr(M) = \lambda_1 + \lambda_2$ and $det(M) = \lambda_1 \lambda_2$ are real. Thus,

- 1. λ_1 and λ_2 are a complex conjugate pair or
- 2. λ_1 and λ_2 are both real.

In the first case, $\lambda_1 = a + ib$ and $\lambda_2 = a - ib$ for some real numbers, a and b, with $b \neq 0$, and hence, $\det(\mathbf{M}) = \lambda_1 \lambda_2 = a^2 + b^2 > 0$ and $\rho = |\lambda_1| = |\lambda_2| = \sqrt{a^2 + b^2}$, i.e., the eigenvalues lie on the circle with radius $\rho = \sqrt{a^2 + b^2} = \sqrt{\det(M)}$. In this case, the first inequality in Eq. (A1) holds since $b \neq 0$ implies

$$|\operatorname{tr}(M)| = 2|a| < 2\rho \le 1 + \rho^2 = 1 + \operatorname{det}(M).$$

Hence, Eq. (A1) is equivalent to $1 + \det(M) < 2$ or $\rho < 1$.

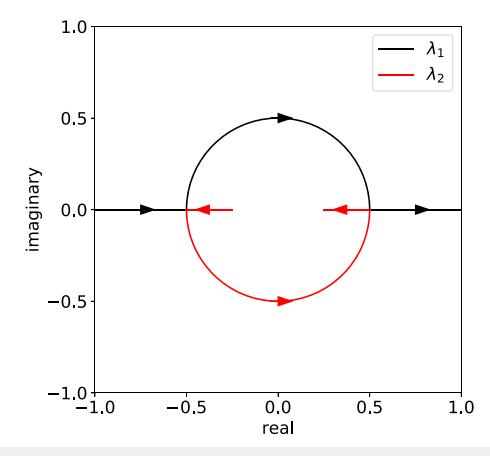


FIG. 7. All possible eigenvalue pairs λ_1 , λ_2 of a matrix **M** that satisfies Eq. (A1) with $\det(\mathbf{M}) = \lambda_1 \lambda_2 = 1/4$ is plotted. The eigenvalue pairs either lie on the circle with radius r = 1/2 or are both real, and in the former case, the spectral radius of M is minimal.

In the second case, λ_1 and λ_2 are both real, and the condition |tr(M)| < 1 + det(M) is equivalent to

$$1 + \lambda_1 \lambda_2 + \lambda_1 + \lambda_2 = (1 + \lambda_1)(1 + \lambda_2) > 0$$

and

$$1 + \lambda_1 \lambda_2 - \lambda_1 - \lambda_2 = (1 - \lambda_1)(1 - \lambda_2) > 0.$$

Together with $det(\mathbf{M}) = \lambda_1 \lambda_2 < 1$, these conditions are equivalent to $\rho = \max(|\lambda_1|, |\lambda_2|) < 1.$

APPENDIX B: STABILITY CONDITION FOR HARMONIC **EXTERNAL POTENTIALS**

This section proves that condition (S3a) implies property (P3), as claimed in Sec. II D. For notational brevity, we define

$$A(x) := \cos(\theta(x)) - \frac{\Delta t^2(\Lambda/m)}{2} \frac{\sin(\theta(x))}{x}.$$

Note that A(x) is equal to $A_{j,n}$ in the display under Eq. (21) if $x = \omega_{i,n} \Delta t$.

Theorem 2. For any $\alpha^* > 0$, (ii) implies (i).

(i) For all $\Lambda \ge 0$, m > 0, and $\Delta t > 0$ satisfying $\Delta t^2 \Lambda / m < \alpha^*$, the function θ satisfies

$$|A(x)| < 1$$
 for $x > 0$.

(ii) The function θ satisfies

$$0 < \theta(x) < 2\arctan(2x/\alpha^*)$$
 for $x > 0$.

Proof. Let $\alpha = \Delta t^2(\Lambda/m)$. For notational brevity, define

$$\phi_{\alpha}(x) := \arctan(\alpha/(2x))$$
 for $x > 0$.

By the harmonic addition identity

$$\cos(\theta) - \tan(\phi_{\alpha})\sin(\theta) = \frac{\cos(\theta + \phi_{\alpha})}{\cos(\phi_{\alpha})},$$

note that (i) can be rewritten as

$$\left| \frac{\cos(\theta(x) + \phi_{\alpha}(x))}{\cos(\phi_{\alpha}(x))} \right| < 1 \quad \text{for } x > 0, \ 0 < \alpha < \alpha^{\star}. \tag{B1}$$

For $0 < \theta(x) < \pi$, Eq. (B1) holds if and only if

$$\phi_{\alpha}(x) < \theta(x) + \phi_{\alpha}(x) < \pi - \phi_{\alpha}(x),$$

which can be rewritten as

$$0 < \theta(x) < 2\arctan(2x/\alpha), \tag{B2}$$

where we used the identity

$$\pi - 2 \arctan(x) = 2 \arctan(1/x)$$
 valid for $x > 0$.

Since arctan is monotonically increasing, and $0 < \alpha < \alpha^*$ by assumption, we may conclude that

$$0 < \theta(x) < 2\arctan(2x/\alpha^*) < 2\arctan(2x/\alpha)$$
.

Thus, if (ii) holds, then Eq. (B2) holds and, therefore, (A1) holds.

Fix $\epsilon \in (0, 1)$. Since Theorem 2 is true for arbitrary α^* , if we take $\alpha^* = 4 - \epsilon$, then the theorem holds with $\Delta t^2 \Lambda/m < 4 - \epsilon$ in Theorem 2 (i) and $\theta(x) < 2\arctan(2x/(4 - \epsilon))$ in Theorem 2 (ii). Since $\epsilon > 0$ is arbitrary, and arctan is monotonically increasing, we can conclude that the theorem holds with $\Delta t^2 \Lambda/m < 4$ and $\theta(x) \le 2\arctan(x/2)$. We therefore have the following corollary of Theorem 2.

Corollary 3. Suppose that the function θ satisfies

$$0 < \theta(x) \le 2 \arctan(x/2)$$
 for $x > 0$.

Then, for all $\Lambda \ge 0$, m > 0, and $\Delta t > 0$ satisfying $\Delta t^2 \Lambda / m < 4$, we have |A(x)| < 1 for x > 0.

APPENDIX C: DIMENSION-FREE QUANTITATIVE CONTRACTION RATE FOR HARMONIC EXTERNAL POTENTIALS IN THE INFINITE-FRICTION LIMIT

In the infinite-friction limit, Eq. (24) simplifies to

$$\mathcal{M}_{j,n} = \mathcal{B}^{1/2} \mathcal{S}_{j,n}^{1/2} \begin{bmatrix} 1 & 0 \\ 0 & 0 \end{bmatrix} \mathcal{S}_{j,n}^{1/2} \mathcal{B}^{1/2}$$

and

$$\mathcal{R}_{j,n} = \frac{1}{\beta m_n} \mathcal{B}^{1/2} \mathcal{S}_{j,n}^{1/2} \begin{bmatrix} 0 & 0 \\ 0 & 1 \end{bmatrix} (\mathcal{B}^{1/2} \mathcal{S}_{j,n}^{1/2})^{\mathrm{T}}.$$

The kth step of the corresponding T-RPMD integrator can be written compactly as

$$\begin{bmatrix} Q_j^{(k)} \\ \varphi_j^{(k)} \end{bmatrix} = \mathcal{M}_{j,n} \begin{bmatrix} Q_j^{(k-1)} \\ \varphi_j^{(k-1)} \end{bmatrix} + \mathcal{R}_{j,n}^{1/2} \begin{bmatrix} \xi_j^{(k-1)} \\ \eta_j^{(k-1)} \end{bmatrix},$$

where $\xi_j^{(k-1)}$ and $\eta_j^{(k-1)}$ are independent standard normal random variables. Suppose that the initial velocity is drawn from the Maxwell–Boltzmann distribution, i.e., $\varphi_j^{(0)} \sim \mathcal{N}(0, (\beta m_n)^{-1})$, and the initial position is drawn from an arbitrary distribution μ_j on \mathbb{R} , i.e., $\varrho_j^{(0)} \sim \mu_j$. Let $p_{j,n}^k$ denote the k-step transition kernel of the position-marginal, i.e., $\mu_j p_{j,n}^k$ is the probability distribution of $\varrho_j^{(k)}$ with $\varrho_j^{(0)} \sim \mu_j$.

Theorem 4 shows that starting from any two initial distributions μ_j and ν_j on \mathbb{R} , the distance between the distributions $\mu_j p_{j,n}^k$ and $\nu_j p_{j,n}^k$ is contractive. We quantify the distance between these distributions in terms of the 2-Wasserstein metric. For two probability distributions μ and ν on \mathbb{R} , the 2-Wasserstein distance between μ and ν is defined as

$$W_2(\mu,\nu) = \left(\inf_{\substack{X \sim \mu \\ Y \sim \nu}} \mathbb{E}(|X - Y|^2)\right)^{1/2},$$

where the infimum is taken over all bivariate random variables (X, Y) such that $X \sim \mu$ and $Y \sim \nu$. ⁵⁴

Theorem 4. Suppose that the function θ satisfies

$$0 < \theta(x) \le 2 \arctan(x/2)$$
 for $x > 0$.

Then, for all k > 1, $\Lambda \ge 0$, m > 0, and $\Delta t > 0$ satisfying $\Delta t^2 \Lambda / m < 4$, and for all initial distributions μ_i and ν_i on \mathbb{R} ,

$$\mathcal{W}_{2}(\mu_{j}p_{j,n}^{k}, \nu_{j}p_{j,n}^{k})$$

$$\leq \begin{cases} A(\omega_{j,n}\Delta t)^{k-1}\mathcal{W}_{2}(\mu_{j}, \nu_{j}) & \text{if } A(\omega_{j,n}\Delta t) > 0\\ \frac{1}{2}\frac{1}{k-1}\mathcal{W}_{2}(\mu_{j}, \nu_{j}) & \text{else.} \end{cases}$$
(C1)

Proof. In the infinite-friction limit, the eigenvalues of $\mathcal{M}_{j,n}$ are $\{0, A(\omega_{j,n}\Delta t)\}$, where A(x) is defined in Appendix B. Let $\varrho_j^{(0)} \sim \mu_j$ and $\tilde{\varrho}_j^{(0)} \sim \nu_j$ be the optimal coupling of μ_j and ν_j , i.e., $\mathcal{W}_2(\mu_j, \nu_j) = \mathbb{E}(|\varrho_j^{(0)} - \tilde{\varrho}_j^{(0)}|^2)^{1/2}$. Conditional on $\varrho_j^{(0)}$ and $\tilde{\varrho}_j^{(0)}$, $\varrho_j^{(k)}$ and $\tilde{\varrho}_j^{(k)}$ are Gaussian random variables with equal variances, but different means. By a well-known result for the 2-Wasserstein distance between Gaussian distributions, 55

$$\mathcal{W}_{2}(\mu_{j}p_{j,n}^{k}, \nu_{j}p_{j,n}^{k})^{2}
= |A(\omega_{j,n}\Delta t)|^{2(k-1)} (\mathcal{M}_{j,n})_{11}^{2} \mathcal{W}_{2}(\mu_{j}, \nu_{j})^{2}
= |A(\omega_{j,n}\Delta t)|^{2(k-1)} \frac{(1 + A(\omega_{j,n}\Delta t))^{2}}{4} \mathcal{W}_{2}(\mu_{j}, \nu_{j})^{2},$$
(C2)

where we used $(\mathcal{M}_{j,n})_{11} = (1 + A(\omega_{j,n}\Delta t))/2$.

Now, we distinguish between two cases. In the case where $A(\omega_{j,n}\Delta t) > 0$, we obtain the required result since $|A(\omega_{j,n}\Delta t)| < 1$ by Corollary 3, and therefore,

$$\frac{\left(1 + A(\omega_{j,n}\Delta t)\right)^2}{4} \le 1. \tag{C3}$$

Otherwise, for $-1 < A(\omega_{j,n}\Delta t) \le 0$, the quantity $|A(\omega_{j,n}\Delta t)|^{2(k-1)} (1 + A(\omega_{j,n}\Delta t))^2$ is maximized at $(-1 + 1/k)^{2k} (k-1)^{-2}$, and therefore,

$$|A(\omega_{j,n}\Delta t)|^{2(k-1)} \frac{(1+A(\omega_{j,n}\Delta t))^2}{4} \le \frac{1}{4(k-1)^2}.$$
 (C4)

Inserting Eqs. (C3) and (C4) into Eq. (C2), and then taking square roots, gives the required result. \Box

APPENDIX D: TOTAL VARIATION BOUND ON THE EQUILIBRIUM ACCURACY ERROR FOR HARMONIC EXTERNAL POTENTIALS

In this section, we show that Eq. (29) follows from conditions (S1a)–(S4a) in the setting of Sec. II E. It is helpful to recall the quantities

$$\omega_{j} = \lim_{n \to \infty} \omega_{j,n} = \begin{cases} \frac{\pi j}{\hbar \beta} & \text{if } j \text{ is even} \\ \frac{\pi (j+1)}{\hbar \beta} & \text{else.} \end{cases}$$
 (D1)

In the following, $\mu_{j,\Delta t}$ and μ_{j} denote the jth factor of the product distributions $\mu_{n,\Delta t}$ and μ_{n} , respectively, introduced in Sec. II E.

Theorem 5. Suppose that the function θ satisfies conditions (S1a)–(S4a). Then, for all $\Lambda \geq 0$, m > 0, and $\Delta t > 0$ satisfying $\Delta t^2 \Lambda/m < 4$, the total variation distance between μ_n and $\mu_{n,\Delta t}$ is bounded as in Eq. (29).

Proof. Subadditivity of the total variation distance $d_{\rm TV}$ between product distributions and its equivalence with the Hellinger distance⁵³ $d_{\rm H}$ lead to the inequalities

$$\begin{split} d_{\text{TV}}(\mu_{n}, \mu_{n,\Delta t})^{2} &\leq \sum_{j=1}^{n-1} d_{\text{TV}}(\mu_{j}, \mu_{j,\Delta t})^{2} \\ &\leq \sum_{j=1}^{n-1} 2 d_{\text{H}}(\mu_{j}, \mu_{j,\Delta t})^{2} \leq \sum_{j=1}^{n-1} \frac{2(s_{j} - s_{j,\Delta t})^{2}}{(s_{j}^{2} + s_{j,\Delta t}^{2})} \\ &\leq \sum_{j=1}^{n-1} \left(1 - \frac{s_{j}}{s_{j,\Delta t}}\right)^{2} \leq \sum_{j=1}^{n-1} \left(1 - \frac{s_{j}^{2}}{s_{j,\Delta t}^{2}}\right)^{2}, \end{split} \tag{D2}$$

where the second-to-last step uses Eq. (28) and the last step uses the elementary inequality $(1 - x^2)^2 \ge (1 - x)^2$ valid for all $x \ge 0$.

Since $\tan(\cdot)$ increases superlinearly on the interval $(0, \pi)$, we have $\theta(x)/2 \le \tan(\theta(x)/2) \le x/2$ for x > 0, where the second inequality uses (S3a). Consequently, the *j*th summand in Eq. (D2) admits the bound

$$\left(1 - \frac{s_j^2}{s_{j,\Delta t}^2}\right)^2 = \left(\frac{\Lambda/m}{\omega_{j,n}^2 + \Lambda/m} \left(\frac{\omega_{j,n}\Delta t/2}{\tan(\theta(\omega_{j,n}\Delta t)/2)} - 1\right)\right)^2 \\
\leq \left(\frac{\Delta t^2 \Lambda/m}{(\omega_{j,n}\Delta t)^2} \left(\frac{\omega_{j,n}\Delta t}{\theta(\omega_{j,n}\Delta t)} - 1\right)\right)^2 \\
\leq \left(\frac{\Delta t^2 \Lambda}{m}\right)^2 \frac{1}{(\omega_{j,n}\Delta t)^2},$$

where the last line uses the lower bound in (S4a). Using that for any even positive integer n,

$$\sum_{j=1}^{n-1} \frac{1}{\omega_{j,n}^2} < \lim_{n \to \infty} \sum_{j=1}^{n-1} \frac{1}{\omega_{j,n}^2} = \sum_{j=1}^{\infty} \frac{1}{\omega_j^2} < \left(\frac{\hbar \beta}{\pi}\right)^2 \sum_{j=1}^{\infty} \frac{2}{j^2},$$

where we used Eq. (D1), the bound in Eq. (D2) becomes

$$d_{\mathrm{TV}}(\mu_n,\mu_{n,\Delta t})^2 < \left(\frac{\Delta t^2 \Lambda}{m}\right)^2 \left(\frac{\hbar \beta}{\pi \Delta t}\right)^2 \sum_{i=1}^{\infty} \frac{2}{j^2}.$$

Taking square roots and using the Riemann zeta function⁶⁴ to evaluate the infinite sum yield Eq. (29).

APPENDIX E: ASYMPTOTIC VARIANCE OF KINETIC ENERGY OBSERVABLES FOR HARMONIC EXTERNAL POTENTIALS IN THE INFINITE-FRICTION LIMIT

In Sec. III A, Figs. 4(b) and 4(d) show that the T-RPMD scheme specified by $\theta(x) = 2 \arctan(x/2)$, which coincides with the Cayley-modified BAOAB scheme introduced in Ref. 43, provides the smallest integrated autocorrelation time [Eq. (31)] for quantum kinetic energy observables [Eq. (30)] among several schemes with properties (P1)–(P5). In this section, we show that this scheme minimizes an upper bound [Eq. (E2)] on the integrated autocorrelation time of the quantum kinetic energy among all dimension-free and strongly stable BAOAB-like schemes for harmonic external potentials.

To this end, note that for a *n*-bead thermostatted ring polymer with external potential $V_n^{\text{ext}}(q) = \frac{\Lambda}{2n} |q|^2$, Eq. (30) can be rewritten as

$$\mathsf{KE}_{n}^{\mathrm{pri}}(\varrho) = \frac{n}{2\beta} - \sum_{j=1}^{n-1} \frac{m_{n}\omega_{j,n}^{2}}{2} \varrho_{j}^{2} \quad \text{and}$$

$$\mathsf{KE}_{n}^{\mathrm{vir}}(\varrho) = \frac{1}{2\beta} + \sum_{i=1}^{n-1} \frac{\Lambda}{2n} \varrho_{j}^{2}, \tag{E1}$$

where ϱ is defined in Eq. (12). In the following, we denote both observables in Eq. (E1) as KE_n and distinguish between the two as needed.

To control the integrated autocorrelation time of KE_n , we need the stationary autocorrelation $Cor(KE_n(\varrho^{(0)}), KE_n(\varrho^{(k\Delta t)}))$ for $k \geq 0$. Note that the distributions of $\varrho^{(k\Delta t)}$ and $\varrho^{(0)}$ are equal by stationarity and that components $(\varrho_j)_{j=0}^{n-1}$ are uncorrelated in a harmonic external potential. Thus,

$$\operatorname{Cor}(\mathsf{KE}_{n}(\varrho^{(0)}), \mathsf{KE}_{n}(\varrho^{(k\Delta t)})) = \sum_{j=1}^{n-1} \chi_{j,n} \operatorname{Cor}(|\varrho_{j}^{(0)}|^{2}, |\varrho_{j}^{(k\Delta t)}|^{2}),$$

where

$$\chi_{j,n} = \frac{\kappa_{j,n}^{2} \text{Var}(|\varrho_{j}^{(0)}|^{2})}{\sum_{i=1}^{n-1} \kappa_{i,n}^{2} \text{Var}(|\varrho_{i}^{(0)}|^{2})}$$

and

$$\kappa_{j,n} = \begin{cases} \frac{m_n \omega_{j,n}^2}{2} & \text{for } \mathsf{KE}_n^{\mathrm{pri}} \\ \frac{\Lambda}{2n} & \text{for } \mathsf{KE}_n^{\mathrm{vir}}. \end{cases}$$

If the evolution of the ring polymer is governed by the BAOAB-like update in Eq. (17), then the jth mode satisfies

$$\operatorname{Cor}(|\varrho_{j}^{(0)}|^{2}, |\varrho_{j}^{(k\Delta t)}|^{2}) = \frac{\operatorname{Cov}(|\varrho_{j}^{(0)}|^{2}, |\varrho_{j}^{(k\Delta t)}|^{2})}{\operatorname{Var}(|\varrho_{j}^{(0)}|^{2})}$$
$$= (\mathcal{M}_{j,n}^{k})_{11}^{2},$$

where we used that the phase $\left[\varrho_{j}^{(k\Delta t)}\ \varphi_{j}^{(k\Delta t)}\right]^{\mathrm{T}}$ follows a centered Gaussian distribution with covariance given in Eq. (26) for all $k\geq 0$. Therefore, in the infinite-friction limit where $\mathcal{M}_{j,n}$ is given in Appendix C, the integrated autocorrelation time of KE_n evaluates to

$$\frac{\operatorname{aVar}(\mathsf{KE}_n)}{\operatorname{Var}(\mathsf{KE}_n)} = 1 + 2 \sum_{j=1}^{n-1} \chi_{j,n} \sum_{k=1}^{\infty} (\mathcal{M}_{j,n}^k)_{11}^2 \\
\leq 1 + \frac{1}{2} \max_{1 \leq j \leq n-1} \left| \frac{1 + A(\omega_{j,n} \Delta t)}{1 - A(\omega_{j,n} \Delta t)} \right|, \tag{E2}$$

where simplification of $(\mathcal{M}_{j,n}^k)_{11}$ was aided by the Cayley–Hamilton theorem for 2×2 matrices, ⁶⁵ A(x) is defined in Appendix B, and in the last line, we used that $\sum_{j=1}^{n-1} \chi_{j,n} = 1$. Equation (E2) states that the integrated autocorrelation time of KE_n can only be as small as that of the component $|\varrho_j|^2$ exhibiting the slowest uncorrelation at stationarity.

Having derived Eq. (E2), we now prove our claim for this section. Let $x := \omega_{j,n} \Delta t > 0$ and $\alpha := \Delta t^2 \Lambda/m \in (0, 4)$. For fixed x and α , the function $A(x) := \cos(\theta(x)) - \frac{\alpha}{2x} \sin(\theta(x))$ monotonically decreases toward -1 as the angle $\theta(x)$ increases toward π . Consequently, the function |(1 + A(x))/(1 - A(x))| decreases (toward 0) as $\theta(x)$ increases (toward π), but condition (S3a) requires $\theta(x) \le 2$ arctan(x/2) to achieve stable evolution. Therefore, as the largest stable angle, the choice $\theta(x) = 2 \arctan(x/2)$ (i.e., the Cayley angle) minimizes the upper bound in Eq. (E2).

A similar argument can be made to support the conjecture, suggested by Fig. 4(f), that the non-centroid velocity estimator for the classical kinetic energy KE_n^{cla} in Eq. (32), equivalently written as

$$KE_n^{cla}(\varphi) = \frac{m_n}{2(n-1)} \sum_{i=1}^{n-1} \varphi_i^2$$
 (E3)

with φ defined in Eq. (12), exhibits a *maximal* integrated autocorrelation time if the Cayley angle $\theta(x) = 2 \arctan(x/2)$ is used. Indeed, the integrated autocorrelation time of this estimator is bounded by

$$\frac{\operatorname{aVar}(\mathsf{KE}_n^{\operatorname{cla}})}{\operatorname{Var}(\mathsf{KE}_n^{\operatorname{cla}})} \le 1 + \frac{1}{2} \max_{1 \le j \le n-1} \left| \frac{1 - A(\omega_{j,n} \Delta t)}{1 + A(\omega_{j,n} \Delta t)} \right|, \tag{E4}$$

where the function |(1 - A(x))/(1 + A(x))| monotonically increases as $\theta(x)$ approaches the largest stable (i.e., Cayley) angle for fixed x and α .

To conclude, we note that the claim proven in this section holds for arbitrary T-RPMD friction schedules despite our use of the infinite-friction limit in Eqs. (E2) and (E4).

APPENDIX F: STABILITY INTERVAL CALIBRATION FOR LIQUID WATER SIMULATIONS

This section describes the computational procedure used to identify $\Delta t = 1.4$ fs as close to the upper bound of the stability interval of T-RPMD applied to q-TIP4P/F liquid water at 298 K and 0.998 g/cm³. The procedure consisted of integrating an ensemble of 10^4 thermally initialized T-RPMD trajectories using the algorithm outlined in Sec. II A in its single-bead realization (identical to velocity Verlet in classical MD⁸) and counting the fraction of trajectories that remained within an energy sublevel (i.e., they did not exhibit detectable energy drift) throughout their duration for each tested time step. A time step was deemed stable if 99% or more of the ensemble remained in an energy sublevel throughout a 50-ps time period. A range of time steps were tested, and the fraction of stable trajectories at each time step is reported in Fig. 8.

To avoid initialization bias in the stability interval estimation, thermalized initial phase-points were generated with a metropolized Markov-chain Monte Carlo sampler targeted at the equilibrium configurational distribution of the liquid. Specifically, a randomized Hamiltonian Monte Carlo 34,66 (rHMC) simulation of sufficient length was used to thermalize a crystalline configuration of the system at the target density, and 10² configurations were extracted from well-separated points along the rHMC trajectory. Each of these approximately independent draws from the equilibrium *configurational* distribution of the liquid at the target physical conditions was subsequently paired with 10² independent velocities drawn from

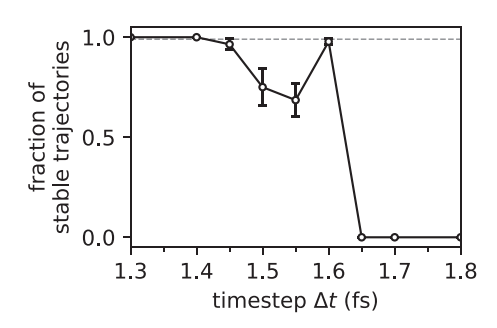


FIG. 8. Stability interval calibration for q-TIP4P/F room-temperature liquid water simulations. Data points correspond to the fraction of thermally initialized single-bead T-RPMD trajectories that remained stable over a 50-ps period at the respective integration time step Δt . The error bars correspond to the standard error of the fraction of stable trajectories across initialization points with different configurations. The gray dashed line marks the \geq 99% threshold for deeming a time step stable, which no time step beyond Δt = 1.4 fs reaches.

the corresponding Maxwell–Boltzmann distribution, yielding 10^4 approximately independent draws from the *phase space* distribution of the classical liquid at thermal equilibrium.

APPENDIX G: SIMULATION AND ESTIMATION DETAILS

This section compiles simulation protocols and statistical estimation methods used to generate Fig. 4 for the one-dimensional quantum harmonic oscillator and Figs. 5 and 6 for room-temperature liquid water.

1. One-dimensional quantum harmonic oscillator

Numerical equilibrium averages and integrated autocorrelation times for the quantum harmonic oscillator were estimated by averaging over a 10-ns T-RPMD trajectory integrated using the algorithm listed in Sec. II A and initialized at an exact sample from the numerical stationary distribution [listed for the jth ring-polymer mode in Eq. (27)] corresponding to the physical parameters (i.e., Λ , m, and β) and simulation parameters (i.e., n, Δt , and the function θ) listed in Sec. III A. Specifically, the statistics reported in Fig. 4 were obtained by partitioning the T-RPMD trajectory into ten disjoint blocks, estimating the equilibrium average and autocorrelation time within each block, and computing the sample mean and standard error among the resulting block estimates with 1000 bootstrap resamples.

We now describe the formulas and methods used to obtain block estimates for the equilibrium mean and integrated autocorrelation time. The equilibrium average μ_{O_n} of observable O_n within each block of the partitioned T-RPMD trajectory was estimated using the standard estimator, ⁶⁷

$$\hat{\mu}_{O_n} = \frac{1}{K} \sum_{k=0}^{K-1} O_n^{(k\Delta t)},$$
 (G1)

where K is the number of steps in the block (i.e., the block size) and $O_n^{(k\Delta t)}$ is the value of O_n at the kth step within the block. Similarly, the lag- $k\Delta t$ autocovariance $C_{O_n}(k\Delta t)$ was estimated using ⁶⁷

$$\hat{C}_{\mathcal{O}_n}(k\Delta t) = \sum_{\ell=0}^{K-k-1} \frac{\left(\mathcal{O}_n^{(\ell\Delta t)} - \hat{\mu}_{\mathcal{O}_n}\right) \left(\mathcal{O}_n^{((\ell+k)\Delta t)} - \hat{\mu}_{\mathcal{O}_n}\right)}{K - k}$$

for $0 \le k\Delta t \le (K-1)\Delta t = 1$ ns. The integrated autocorrelation time was subsequently estimated using 58,67

$$\frac{\widehat{\operatorname{aVar}_{O_n}}}{\operatorname{Var}_{O_n}}(M) = 1 + 2\sum_{k=1}^{M} \frac{\widehat{C}_{O_n}(k\Delta t)}{\widehat{C}_{O_n}(0)},$$
 (G2)

where $0 < M \le K$ is a suitable cutoff. The choice of M is nontrivial, as it carries a trade-off between the bias (more pronounced at small M) and variance (more pronounced at large M) of the estimator. To choose M judiciously, we follow the *automatic windowing* (AW) method described in Appendix C of Ref. 68. The AW method dictates that M should correspond to the smallest lag that satisfies the inequality

$$M \ge c \, \widehat{\frac{aVar_{O_n}}{Var_{O_n}}}(M),$$

where the parameter c > 0 dictates the variance–bias trade-off in place of M and is chosen as large as possible to reduce the bias of the estimator for a given variance threshold.

Figure 9 illustrates the usage of the AW method for integrated autocorrelation time estimation with trajectory data generated by the BAOAB-like T-RPMD scheme with $\theta(x) = 2 \arctan(x/2)$ at n = 64 beads and $\Delta t = 2.0$ fs, focusing on the observables $\mathsf{KE}_n^{\mathsf{pri}}$ (black), $\mathsf{KE}_n^{\mathsf{vir}}$ (red), and $\mathsf{KE}_n^{\mathsf{cla}}$ (cyan), introduced in Sec. III A. The estimated integrated autocorrelation times are plotted with solid lines in Fig. 9(a) for various values of c, and the corresponding cutoffs M are plotted in Fig. 9(b). Exact integrated autocorrelation times are plotted with dashed lines in Fig. 9(a). Note that as c (and thus d) increases, the estimates converge to the corresponding exact values at the expense of a larger variance, which can nonetheless be controlled by adjusting the block size K.

2. Room-temperature liquid water

The equilibrium averages and integrated autocorrelation times reported in Fig. 5 were obtained by averaging over 10-ns T-RPMD trajectories integrated for each considered bead number n, time step Δt , and function θ . All trajectories were initialized at an approximate sample from the corresponding numerical equilibrium distribution, obtained by thermalizing for 20 ps a classical (i.e., n=1) configuration of the system into the n-bead ring-polymer phase space. Figure 10 checks that this thermalization protocol indeed leads to near-equilibrium initialization of the T-RPMD trajectories. The reference equilibrium averages plotted with dashed lines in Fig. 5 were obtained by averaging over a one-nanosecond, 256-bead staging PIMD²⁸ trajectory integrated at a 0.1-fs time step with the mass and friction parameters recommended in Ref. 30 and initialized with the same protocol used for the T-RPMD simulations.

The observables considered in Fig. 5 measure properties per H atom or per H_2O molecule, and thus, the reported values are

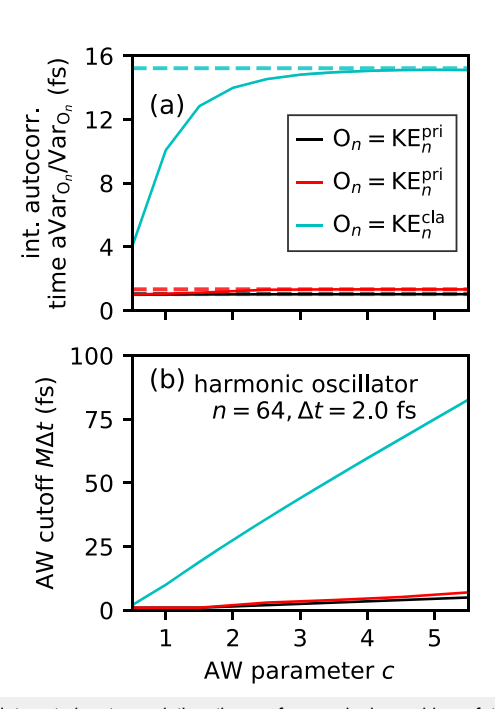


FIG. 9. Integrated autocorrelation times of several observables of the one-dimensional harmonic oscillator in Sec. III A, estimated with the AW method. Trajectory data for the estimates were generated using the T-RPMD scheme with $\theta(x) = 2 \arctan(x/2)$ at n = 64 beads and $\Delta t = 2.0$ fs and processed as described in the current section. Estimated (respectively, exact) integrated autocorrelation times for observables, $KE_n^{\rm pri}$ (black), $KE_n^{\rm vir}$ (red), and $KE_n^{\rm cla}$ (cyan), are shown in solid (respectively, dashed) lines in panel (a) as a function of the windowing parameter c. Panel (b) plots the cutoffs determined by the choice of c for the three observables, where the linear relation between $M\Delta t$ and c at large values of the latter corroborates the convergence of the autocorrelation time estimates

averages over estimates obtained for each simulated moiety. The equilibrium mean and integrated autocorrelation time of observable O_n for each moiety were estimated by partitioning the trajectory of the moiety into ten disjoint 1-ns blocks, evaluating Eqs. (G1) and (G2) within each block, and determining the sample mean and standard error among the block estimates with 1000 bootstrap resamples. The AW method⁶⁸ was applied to choose a cutoff lag $M \le 1$ ns in Eq. (G2), as illustrated in Fig. 9 for the harmonic oscillator application.

The T-RPMD trajectories used to generate Fig. 5 also yielded Fig. 6, where panels (a) and (c) plot autocovariance functions of the form $\frac{1}{N_{\rm H_2O}}\sum_{i=1}^{N_{\rm H_2O}}\mathbb{E}(\bar{O}_i(0)\cdot\bar{O}_i(k\Delta t))$, where $N_{\rm H_2O}=32$ is the number of simulated H₂O molecules and $\bar{O}_i(k\Delta t)$ is the bead-averaged value of observable O (e.g., the molecular dipole moment or center-of-mass velocity) on the *i*th molecule at time $k\Delta t$ along a stationary T-RPMD trajectory. The autocovariance $\mathbb{E}(\bar{O}_i(0)\cdot\bar{O}_i(t))$ was estimated for the lags $k\Delta t$ shown in Figs. 6(a) and 6(c) by

$$\mathbb{E}\big(\bar{\mathsf{O}}_i(0)\cdot\bar{\mathsf{O}}_i(k\Delta t)\big)\approx\sum_{\ell=0}^{K-k-1}\frac{\bar{\mathsf{O}}_i^{(\ell\Delta t)}\cdot\bar{\mathsf{O}}_i^{((\ell+k)\Delta t)}}{K-k},$$

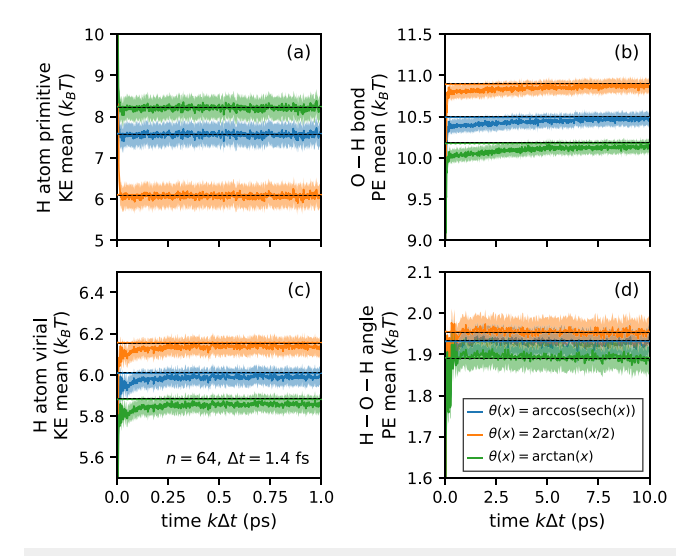


FIG. 10. Convergence to equilibrium of the BAOAB-like schemes considered in Sec. III B with n=64 ring-polymer beads and a $\Delta t=1.4$ fs time step. With respect to the non-equilibrium 64-bead configurational distribution evolved from a point mass at a classical (i.e., n=1) configuration, panels (a) and (c) plot the mean kinetic energy per H atom for the n-bead system as per the primitive and virial estimators, respectively, for times up to 1.0 ps. Panels (b) and (d), respectively, plot the non-equilibrium mean O–H-bond and H–O–H-angle potential energy per q-TIP4P/F water molecule for times up to 10 ps. The lightly shaded interval around each curve corresponds to the standard error of the estimated non-equilibrium mean, computed with 1000 bootstrap resamples from a sample of 1000 independent trajectories.

where $K\Delta t = 1$ ns is the length of each block in a partitioned 10-ns T-RPMD trajectory. As with the results in Fig. 5, statistics for each molecule were obtained from block estimates via bootstrapping, and Figs. 6(a) and 6(c) report molecule-averaged statistics.

Figure 10 validates the 20-ps thermalization interval used to initialize the trajectories that generated Figs. 5 and 6. In detail, Figs. 10(a) and 10(c) [respectively, Figs. 10(b) and 10(d)] plot the non-equilibrium mean of the primitive and virial quantum kinetic energy per H atom (respectively, the mean O-H bond and H-O-H angle potential energy per water molecule) as it approaches the equilibrium value in Figs. 5(a) and 5(c) [respectively, Figs. 5(e) and 5(g)] for a 64-bead ring polymer at a 1.4 fs time step with the considered choices of θ . At each time $k\Delta t$ within the 20-ps interval, the non-equilibrium mean is estimated by averaging across 1000 independent trajectories initialized at a point-mass distribution on the n-bead ring-polymer phase space centered at the classical (i.e., n = 1) sample used to initialize the reported simulations. Within statistical uncertainty, the non-equilibrium mean for each observable converges to its equilibrium value within the 20-ps interval at visually indistinguishable rates across the tested choices of θ .

DATA AVAILABILITY

The data that support the findings of this study are available from the corresponding author upon reasonable request.

REFERENCES

- ¹M. Parrinello and A. Rahman, "Study of an *F* center in molten KCl," J. Chem. Phys. **80**, 860–867 (1984).
- ²S. Habershon, D. E. Manolopoulos, T. E. Markland, and T. F. Miller III, "Ring-polymer molecular dynamics: Quantum effects in chemical dynamics from classical trajectories in an extended phase space," Annu. Rev. Phys. Chem. **64**, 387–413 (2013)
- ³T. E. Markland and M. Ceriotti, "Nuclear quantum effects enter the mainstream," Nat. Rev. Chem. 2, 0109 (2018).
- ⁴R. P. Feynman, *Quantum Mechanics and Path Integrals*, 1st ed. (McGraw-Hill, 1965).
- ⁵D. Chandler and P. G. Wolynes, "Exploiting the isomorphism between quantum theory and classical statistical mechanics of polyatomic fluids," J. Chem. Phys. **74**, 4078–4095 (1981).
- ⁶D. Frenkel and B. Smit, *Understanding Molecular Simulation: From Algorithms to Applications*, 2nd ed. (Academic Press, 2002).
- ⁷D. C. Rapaport, *The Art of Molecular Dynamics Simulation*, 2nd ed. (Cambridge University Press, UK, 2004).
- ⁸B. Leimkuhler and C. Matthews, *Molecular Dynamics*, Interdisciplinary Applied Mathematics Vol. 39, 1st ed. (Springer International Publishing, 2015).
- ⁹M. P. Allen and D. J. Tildesley, *Computer Simulation of Liquids*, 2nd ed. (Oxford University Press, 2017).
- ¹⁰ J. Cao and G. A. Voth, "The formulation of quantum statistical mechanics based on the Feynman path centroid density. II. Dynamical properties," J. Chem. Phys. 100, 5106–5117 (1994).
- ¹¹I. R. Craig and D. E. Manolopoulos, "Quantum statistics and classical mechanics: Real time correlation functions from ring polymer molecular dynamics," J. Chem. Phys. 121, 3368–3373 (2004).
- ¹²J. Liu, "Path integral Liouville dynamics for thermal equilibrium systems," J. Chem. Phys. **140**, 224107 (2014).
- ¹³T. J. H. Hele, M. J. Willatt, A. Muolo, and S. C. Althorpe, "Boltzmann-conserving classical dynamics in quantum time-correlation functions: 'Matsubara dynamics'," J. Chem. Phys. **142**, 134103 (2015).
- ¹⁴T. J. H. Hele, M. J. Willatt, A. Muolo, and S. C. Althorpe, "Communication: Relation of centroid molecular dynamics and ring-polymer molecular dynamics to exact quantum dynamics," J. Chem. Phys. **142**, 191101 (2015).
- ¹⁵J. R. Cendagorta, Z. Bačić, and M. E. Tuckerman, "An open-chain imaginary-time path-integral sampling approach to the calculation of approximate symmetrized quantum time correlation functions," J. Chem. Phys. 148, 102340 (2018).
- ¹⁶I. R. Craig and D. E. Manolopoulos, "Chemical reaction rates from ring polymer molecular dynamics," J. Chem. Phys. 122, 084106 (2005).
- ¹⁷I. R. Craig and D. E. Manolopoulos, "A refined ring polymer molecular dynamics theory of chemical reaction rates," J. Chem. Phys. **123**, 034102 (2005).
- ¹⁸T. F. Miller III and D. E. Manolopoulos, "Quantum diffusion in liquid water from ring polymer molecular dynamics," J. Chem. Phys. 123, 154504 (2005)
- ¹⁹T. F. Miller III and D. E. Manolopoulos, "Quantum diffusion in liquid *para*-hydrogen from ring-polymer molecular dynamics," J. Chem. Phys. **122**, 184503 (2005).
- ²⁰S. Habershon, G. S. Fanourgakis, and D. E. Manolopoulos, "Comparison of path integral molecular dynamics methods for the infrared absorption spectrum of liquid water," J. Chem. Phys. **129**, 074501 (2008).
- ²¹ A. Witt, S. D. Ivanov, M. Shiga, H. Forbert, and D. Marx, "On the applicability of centroid and ring polymer path integral molecular dynamics for vibrational spectroscopy," J. Chem. Phys. 130, 194510 (2009).
- ²²J. A. Morrone and R. Car, "Nuclear quantum effects in water," Phys. Rev. Lett. 101, 017801 (2008).
- ²³B. Cheng, E. A. Engel, J. Behler, C. Dellago, and M. Ceriotti, "*Ab initio* thermodynamics of liquid and solid water," Proc. Natl. Acad. Sci. U. S. A. **116**, 1110–1115 (2019)
- ²⁴T. Zimmermann and J. Vaníček, "Path integral evaluation of equilibrium isotope effects," J. Chem. Phys. 131, 024111 (2009).
- ²⁵D. L. Eldridge, R. Korol, M. K. Lloyd, A. C. Turner, M. A. Webb, T. F. Miller III, and D. A. Stolper, "Comparison of experimental vs theoretical abundances

- of $^{13}\text{CH}_3\text{D}$ and $^{12}\text{CH}_2\text{D}_2$ for isotopically equilibrated systems from 1 to 500 °C," ACS Earth Space Chem. 3, 2747–2764 (2019).
- ²⁶H. F. Trotter, "On the product of semi-groups of operators," Proc. Am. Math. Soc. 10, 545–551 (1959).
- ²⁷G. Strang, "On the construction and comparison of difference schemes," SIAM J. Numer. Anal. 5, 506–517 (1968).
- ²⁸ M. E. Tuckerman, B. J. Berne, G. J. Martyna, and M. L. Klein, "Efficient molecular dynamics and hybrid Monte Carlo algorithms for path integrals," J. Chem. Phys. **99**, 2796–2808 (1993).
- ²⁹ M. Ceriotti, M. Parrinello, T. E. Markland, and D. E. Manolopoulos, "Efficient stochastic thermostatting of path integral molecular dynamics," J. Chem. Phys. 133, 124104 (2010).
- ³⁰ J. Liu, D. Li, and X. Liu, "A simple and accurate algorithm for path integral molecular dynamics with the Langevin thermostat," J. Chem. Phys. **145**, 024103 (2016).
- ³¹M. P. Calvo and J. M. Sanz-Serna, "Instabilities and inaccuracies in the integration of highly oscillatory problems," SIAM J. Sci. Comput. **31**, 1653–1677 (2009).
- ³²V. I. Arnol'd, Mathematical Methods of Classical Mechanics, Graduate Texts in Mathematics Vol. 60, 2nd ed. (Springer Science & Business Media, 2013).
- ³³ P. Minary, G. J. Martyna, and M. E. Tuckerman, "Algorithms and novel applications based on the isokinetic ensemble. I. Biophysical and path integral molecular dynamics," J. Chem. Phys. 118, 2510–2526 (2003).
- ³⁴ N. Bou-Rabee and J. M. Sanz-Serna, "Geometric integrators and the Hamiltonian Monte Carlo method," Acta Numer. 27, 113–206 (2018).
- ³⁵N. Bou-Rabee and A. Eberle, "Two-scale coupling for preconditioned Hamiltonian Monte Carlo in infinite dimensions," Stochastics Partial Differ. Equations: Anal. Comput. (published online, 2020).
- ³⁶J. Lu, Y. Lu, and Z. Zhou, "Continuum limit and preconditioned Langevin sampling of the path integral molecular dynamics," J. Comput. Phys. 423, 109788 (2020).
- ³⁷M. Ceriotti, D. E. Manolopoulos, and M. Parrinello, "Accelerating the convergence of path integral dynamics with a generalized Langevin equation," J. Chem. Phys. **134**, 084104 (2011).
- ³⁸M. Rossi, M. Ceriotti, and D. E. Manolopoulos, "How to remove the spurious resonances from ring polymer molecular dynamics," J. Chem. Phys. **140**, 234116 (2014).
- ³⁹Z. Zhang, X. Liu, Z. Chen, H. Zheng, K. Yan, and J. Liu, "A unified thermostat scheme for efficient configurational sampling for classical/quantum canonical ensembles via molecular dynamics," J. Chem. Phys. **147**, 034109 (2017).
- ⁴⁰ M. Rossi, V. Kapil, and M. Ceriotti, "Fine tuning classical and quantum molecular dynamics using a generalized Langevin equation," J. Chem. Phys. 148, 102301 (2018).
- ⁴¹R. Korol, N. Bou-Rabee, and T. F. Miller III, "Cayley modification for strongly stable path-integral and ring-polymer molecular dynamics," J. Chem. Phys. **151**, 124103 (2019).
- ⁴²B. J. Braams and D. E. Manolopoulos, "On the short-time limit of ring polymer molecular dynamics," J. Chem. Phys. **125**, 124105 (2006).
- ⁴³ R. Korol, J. L. Rosa-Raíces, N. Bou-Rabee, and T. F. Miller III, "Dimension-free path-integral molecular dynamics without preconditioning," J. Chem. Phys. 152, 104102 (2020).
- ⁴⁴G. Bussi, D. Donadio, and M. Parrinello, "Canonical sampling through velocity rescaling," J. Chem. Phys. **126**, 014101 (2007).
- ⁴⁵B. Leimkuhler and C. Matthews, "Rational construction of stochastic numerical methods for molecular sampling," Appl. Math. Res. Express 2013, 34–56.
- ⁴⁶N. Bou-Rabee, "Time integrators for molecular dynamics," Entropy **16**, 138–162 (2014).
- ⁴⁷Y. Fang, Y. Cao, and R. D. Skeel, "Quasi-reliable estimates of effective sample size," IMA Journal of Numerical Analysis (published online).

- ⁴⁸The function $\theta(x) = \arccos(\operatorname{sech}(x))$ is not differentiable at the origin and hence, strictly speaking, does not satisfy condition (S1a). Moreover, the function has even symmetry and hence fails to yield a reversible free ring-polymer update. These formal shortcomings can be fixed by multiplying the function by $\operatorname{sign}(x)$, which we implicitly do for this and other functions θ with similar features.
- 49 G. Metafune, D. Pallara, and E. Priola, "Spectrum of Ornstein-Uhlenbeck operators in L^p spaces with respect to invariant measures," J. Funct. Anal. **196**, 40–60 (2002).
- 50 G. A. Pavliotis, *Stochastic Processes and Applications*, Texts in Applied Mathematics Vol. 60 (Springer, 2014).
- ⁵¹J. M. Sanz-Serna and M. P. Calvo, *Numerical Hamiltonian Problems*, Applied Mathematics and Mathematical Computation Vol. 7, 1st ed. (Chapman & Hall, 1994)
- ⁵²Condition (S3a) may be viewed as a relaxation of the sufficient condition for ergodicity given in Eq. (18) of Ref. 43. Indeed, condition (S3a) implies ergodicity irrespective of the Ornstein–Uhlenbeck friction schedule, whereas Eq. (18) in Ref. 43 does not imply ergodicity for friction schedules that lead to overdamped dynamics.
- $^{5\dot{3}}$ A. L. Gibbs and F. E. Su, "On choosing and bounding probability metrics," Int. Stat. Rev. 70, 419–435 (2002).
- ⁵⁴C. Villani, Optimal Transport: Old and New, Comprehensive Studies in Mathematics Vol. 338 (Springer Science & Business Media, 2008).
- ⁵⁵C. R. Givens and R. M. Shortt, "A class of Wasserstein metrics for probability distributions," Mich. Math. J. 31, 231–240 (1984).
- ⁵⁶S. Habershon, T. E. Markland, and D. E. Manolopoulos, "Competing quantum effects in the dynamics of a flexible water model," J. Chem. Phys. 131, 024501 (2009).
- $^{57}\mathrm{C.}$ J. Geyer, "Practical Markov chain Monte Carlo," Stat. Sci. 7, 473–483 (1992).
- ⁵⁸ A. Sokal, "Monte Carlo methods in statistical mechanics: Foundations and new algorithms," in *Functional Integration: Basics and Applications*, edited by C. DeWitt-Morette, P. Cartier, and A. Folacci (Springer Science & Business Media, Boston, MA, 1997), pp. 131–192.
- ⁵⁹S. Asmussen and P. W. Glynn, Stochastic Simulation: Algorithms and Analysis, Stochastic Modelling and Applied Probability Vol. 57, 1st ed. (Springer, 2007).
- ⁶⁰R. Skeel and Y. Fang, "Comparing Markov chain samplers for molecular simulation," Entropy 19, 561 (2017).
- ⁶¹Y. Fang, Y. Cao, and R. D. Skeel, "Quasi-reliable estimates of effective sample size," arXiv:1705.03831 (2017).
- ⁶²Y. V. Suleimanov, J. W. Allen, and W. H. Green, "RPMDrate: Bimolecular chemical reaction rates from ring polymer molecular dynamics," Comput. Phys. Commun. 184, 833–840 (2013).
- ⁶³ V. Kapil, M. Rossi, O. Marsalek, R. Petraglia, Y. Litman, T. Spura, B. Cheng, A. Cuzzocrea, R. H. Meißner, D. M. Wilkins, B. A. Helfrecht, P. Juda, S. P. Bienvenue, W. Fang, J. Kessler, I. Poltavsky, S. Vandenbrande, J. Wieme, C. Corminboeuf, T. D. Kühne, D. E. Manolopoulos, T. E. Markland, J. O. Richardson, A. Tkatchenko, G. A. Tribello, V. Van Speybroeck, and M. Ceriotti, "i-PI 2.0: A universal force engine for advanced molecular simulations," Comput. Phys. Commun. 236, 214–223 (2019).
- ⁶⁴M. Abramowitz and I. A. Stegun, *Handbook of Mathematical Functions, with Formulas, Graphs, and Mathematical Tables*, 1st ed. (Dover Publications, Inc., USA, 1965).
- $^{\mathbf{65}}\mathrm{T.}$ Andreescu, Essential Linear Algebra with Applications, 1st ed. (Birkhäuser Basel, 2016).
- ⁶⁶N. Bou-Rabee and J. M. Sanz-Serna, "Randomized Hamiltonian Monte Carlo," Ann. Appl. Probab. 27, 2159–2194 (2017).
- $^{\bf 67}$ M. B. Priestly, Spectral Analysis and Time Series, 1st ed. (Academic Press, UK, 1981).
- ⁶⁸ N. Madras and A. D. Sokal, "The pivot algorithm: A highly efficient Monte Carlo method for the self-avoiding walk," J. Stat. Phys. **50**, 109–186 (1988).